Full length article

The effect of solid solution and gamma prime on the deformation modes in Ni-based superalloys

Allan Harte[a,*], Michael Atkinson[a], Albert Smith[a], Carsten Drouven[b], Stefan Zaefferer[c], João Quinta da Fonseca[a], Michael Preuss[a]

[a] School of Materials, The University of Manchester, Oxford Road, Manchester, M13 9PL, United Kingdom
[b] Institute of Physical Metallurgy and Metal Physics, RWTH Aachen University, 52056 Aachen, Germany
[c] Max-Planck-Institut für Eisenforschung GmbH, Max-Planck-Str. 1, 40237 Düsseldorf, Germany

ARTICLE INFO

ABSTRACT

Understanding the deformation, strengthening and failure mechanisms in polycrystalline nickel-base superalloys is necessary to develop next generation alloys for application in highly demanding environments. Here, the aim is to examine the various ways in which solution- and γ' precipitation-strengthening affect the deformation behaviour of three Ni-based superalloys through deformation mapping and investigation at multiple length-scales. This is achieved using high-resolution digital image correlation to quantify local strain, electron backscattered diffraction for lattice rotations and electron channelling contrast imaging to investigate dislocation-mediated mechanisms of deformation. This approach bridges the gap between nano-scale microscopy of dislocation-γ' interactions and macro-scale measurements of mechanical properties, such as yield stress, flow stress and the strain-hardening rate. Deformation in solution-strengthened alloys progresses by a slip band refinement mechanism, which results in low levels of dislocation pileup at grain boundaries and so better grain deformation compatibility with neighbours. Deformation in the γ'-strengthened alloys evolves through a glide plane softening mechanism and the resulting high strain localisation impinges on grain boundaries, creating diffuse strain regions at the boundary. In the coarse-γ' variant there is more Orowan looping and cross slip around larger precipitates, more slip planes are active and more grain-scale cross slip takes place, resulting in greater local friction stresses and therefore greater macroscopic flow stresses and strain-hardening rates. We provide evidence of greater interaction between intersecting non co-planar slip bands in the γ'-strengthened alloys, which contributes to the strain-hardening by progressively decreasing the slip distance. This mechanism is not observed in the solution-strengthened alloy.

1. Introduction

In polycrystalline precipitation-hardened Ni-based superalloys, the microstructure commonly consists of an fcc γ phase matrix and a high volume fraction of L1$_2$ γ'. This microstructure is essential for the high temperature mechanical properties of current generation aero engine components, such as high-pressure turbine discs [1]. The precipitation-strengthened alloy RR1000 was developed as an improvement to Udimet® 720Li for better strength, improved damage tolerance and creep resistance [2]. RR1000 is usually processed to display a complex, multimodal spherical γ' distribution. In order to understand the individual contributions of γ' in different size regimes, previous groups have developed unimodal γ' size distributions and investigated various mechanical testing regimes [3–14];

neutron diffraction experiments were employed to measure the elastic strain response of γ and γ' and transmission electron microscopy (TEM) investigations to derive the dislocation-mediated mechanisms responsible for the mechanical behaviour [15]. In general, it is agreed that deformation proceeds by shearing of smaller particles by coupled dislocations [3] and by bypassing larger particles by Orowan looping [16]; models are able to capture the strengthening due to these mechanisms reasonably well [17].

The performance of a polycrystalline material and its localised failure depend on the strain localisation and how this interacts with the microstructure, with controlling factors being the grain size, the texture, the phases present and the deformation substructures [18]. Whilst the interactions between dislocations and γ' are well understood, there is a lack of understanding in how such interactions contribute towards strain localisation and, ultimately, alloy performance under various loading conditions such as monotonic mechanical load, cyclic fatigue, long-term creep and dynamic crack

Table 1
Nominal alloy compositions for RR1000 and Inconel 690 [97].

Alloy	Cr	Co	Fe	Mo	Nb	Al	Ti	Ta	Hf	C	B	Zr	Ni
RR1000	15.0	18.5	–	5.0	1.1	3.0	3.6	2.0	0.5	0.027	0.015	0.06	Bal
Inconel 690	29.0	–	9.0	–	–	–	–	–	–	0.025	–	–	Bal

growth. This is because TEM investigations are commonly used to explore mechanisms of dislocation-microstructure interaction [19–25]. TEM, however, although it provides high spatial resolution and crystallographic information, it can only give limited information regarding the magnitude and the history of the local deformation. Furthermore, stress and strain artefacts may be introduced by sample thinning and the representativeness of data from small volumes is questionable. In this paper we aim to bridge these shortcomings by imaging dislocations directly in the regions from which measures of deformation are quantified.

The primary way by which deformation proceeds in metals and alloys is through dislocation glide within localised slip bands. The measurement of strain associated with slip traces, their interaction with microstructural features and their contribution to local failure is a topic of on-going investigation using strain mapping techniques and multi-scale direct observations with electron channelling contrast imaging (ECCI) and TEM [26–32]. The high magnitude of lattice distortion at grain boundaries is well known [33–38] and is consistent with Ashby's explanation of GND pile up at grain boundaries to result in local lattice misorientation [39] and backstresses that contribute to local slip resistance [40]. However, there are other ways in which lattice misorientation can occur at grain boundaries. For instance, slip band impingement on a grain boundary can cause lattice misorientation in the neighbouring grain close to the boundary [41,42], which is especially prevalent if slip transmission is not favourable [42]. Further, special types of boundaries, such as the $\Sigma 3$ annealing twin boundaries, and their interaction with high angle grain boundaries are known to be important in strain localisation that develop towards fatigue crack initiation sites [43]. An understanding of these interactions can be approached by coupling high resolution digital image correlation (HRDIC) to measure plastic history with electron backscatter diffraction (EBSD) to measure local lattice rotation [26].

In the present work, our aim is to investigate quantitatively the effect of the presence and size of γ' strengthening particles on strain localisation, local deformation mechanisms and mechanical properties. This is achieved by employing automated data collection routines for HRDIC [44] and EBSD [45] techniques to obtain correlative, quantitative measures of plastic strain localisation and lattice distortion. The lateral resolution of these data presented here after post-processing image and orientation data from the scanning electron microscope (SEM) is on the order of 100 nm for the HRDIC strain data and 500 nm for the EBSD orientation data. The field of view has a size of ~1 × 0.5 mm². This approach allows a quantitative and statistical, representative description of the deformation microstructure, the mechanisms involved in deformation and how their strain localisation contributes to mechanical properties such as yield stress, flow stress and the rate of strain-hardening. The dislocation-mediated nanoscale mechanisms that contribute to the local deformation character are investigated using site-specific diffraction-controlled (c)ECCI with a lateral resolution of ~10 nm in the SEM [46]. cECCI allows to observe and analyse extended lattice defects in a way similar to scanning transmission electron microscopy (STEM) but with the significant advantage that bulk samples can be observed. The correlative approach taken here allows us to image individual dislocations and their interaction with the microstructure at specific deformation regions of interest selected from the HRDIC and EBSD data. In doing so, we are able to build a picture of the effect of the presence and size of γ' on the nano-scale deformation mechanisms and how this contributes to the strain localisation and macroscopic mechanical properties that are measured at the meso- and macro-scale.

2. Experimental

2.1. Material

The alloys investigated here were Inconel 690, a purely solution-strengthened Ni superalloy, and γ'-strengthened RR1000, heat-treated to produce either fine- or coarse-sized γ'. The nominal alloy compositions for Inconel 690 and RR1000 are given in Table 1. The heat treatments for the modified RR1000 were carried out on 20 × 20 × 100 mm blocks and followed procedures described in [14]. These procedures resulted in either the unimodal coarse-γ' or near unimodal fine-γ' microstructure.

2.2. Precipitate characterisation

In order to characterize the morphology of γ' precipitates some samples were polished with successive mechanical grinding and polishing steps, finishing with 0.06 μm colloidal silica, and then etched using a two-part etchant. Etchant part 1 was made of 150 ml H_2O, 150 ml HCL and 2.5 g MoO_3. Etchant part 2 was made of 15 ml HNO_3 and 25 ml H_2O. To make the combined etchant, part 2 was added to 30 ml of part 1. The etching procedure removed the γ' precipitates and remaining structures were imaged in a FEI Sirion FEG-SEM using a through -lens secondary electron detector in ultra high resolution mode.

2.3. Orientation mapping

Orientation mapping was performed in the region of interest using a FEG-SEM (Zeiss Sigma) equipped with an Oxford Instruments electron backscatter diffraction (EBSD) system, consisting of a NordlyNano detector and Aztec software version 3. Scans were performed at an operating voltage of 30 kV and a probe current of ~7.8 nA using the 120 μm aperture in high current mode. An area of ~1 × 0.5 mm was scanned with a step size of 0.5 μm at an acquisition rate of ~35 Hz. The Oxford Instruments Aztec software was used for Hough transform-based indexing of diffraction patterns. All orientation mapping was performed in the deformed state after removal of the gold speckle with a very light mechanical polish using 60 nm colloidal silica for approximately 60 s. The EBSD data, together with the HRDIC data, for all three alloys are available for download [47–49].

2.4. High resolution digital image correlation

2.4.1. Gold remodelling

A gold speckle was applied to the polished sample surface using the gold remodelling technique [44]. A 25–40 nm thick gold layer was deposited onto the sample surface using an Edwards S150B sputter coater at a rate of 5–8 nm min^{-1}. Following this, the remodelling was performed in a water vapour environment for 3 hr.

2.4.2. Image acquisition

Backscattered electron images (BSEI) of the gold speckle pattern were obtained before and after the deformation step using a FEI Magellan HR 400 L FEG-SEM. BSEI are preferred over secondary electron images because the high compositional contrast between the gold and the nickel provides well-defined features for tracking and the BSEI do not suffer as much from contrast changes due to carbon

contamination and surface relief caused by deformation. To maximise the lateral resolution, the microscope was operated at a voltage of 5 kV with $a + 2$ kV stage bias and a probe current of 0.8 nA. A working distance of 4 mm was chosen to maximise the signal-to-noise ratio. A mosaic of 40 columns x 20 rows was used to collect 800 images with a 20% overlap, corresponding to a field of view of $\sim 1 \times 0.5$ mm. Each image had a pixel resolution of 2048×1768 pixels with a pixel size of 14.6 nm. After the deformation step, great care was taken to ensure that the contrast and brightness of the post-deformation images closely represented those in the non-deformed state in order to minimise systematic error.

2.4.3. Mechanical testing

Dogbone samples were machined for tensile testing and microstructural characterisation by electric discharge machining (EDM). The samples were 50 mm in length and 1 mm thick, with tabs of dimensions 10×10 mm and a gauge length of 30 mm. The EDM recast layer was removed by grinding and the sample surface polished with the final step being colloidal silica (0.06 μm) for ~ 10 min. The dogbone samples were deformed in monotonic uniaxial tension to failure on an Instron 5569 10 kN loadcell at an initial strain rate of 1.6×10^{-4} s^{-1}. The displacement was monitored with an MTS extensometer to failure. This provided full stress-strain data to fracture, and the point of fracture was captured within the gauge length measured by the extensometer. For HRDIC, the dogbone samples were deformed under monotonic uniaxial tension using a Kammrath & Weiss 5 kN tension-compression microtester. The sample was deformed at a rate of 1.6×10^{-4} s^{-1} to a global macroscopic uniaxial engineering strain of ~ 0.02. After deformation, the sample was removed from the tensile testing device and post-deformation images of the gold speckle pattern were obtained in the unloaded state as described in Section 2.4.2. Then, the gold speckle pattern was removed prior to post-deformation orientation mapping and cECCI investigation of dislocation structures.

2.4.4. Image correlation

The image mosaics were stitched together using the Grid/Collection stitching plugin for FIJI [50] and cropped into 8 separate areas for image correlation due to computer memory limitations. The stitched images from the deformed and non-deformed state were correlated using LaVision's commercially available DIC software, DaVis 8 [51]. The systematic error was calculated by comparing two images in the non-deformed state. These images were from the same region but the sample was removed from the microscope and replaced before taking the second image. The two images were then correlated using decreasing interrogation window sizes to optimise the size [44]. It was found that using a sub-window size of 8×8 pixels and no overlap resulted in the best resolution whilst keeping the systematic error below an effective strain of 0.01. The uncertainty in strain measurement is therefore $\varepsilon_{eff} \sim 0.01$ (Eq. (2)) for a strain map lateral resolution of 117 nm. Hence, the lateral resolution of our measurements of strain is limited by an initial "gauge length" of 117 nm. While this means that slip bands separated by a distance less than 117 nm are observed as a single trace, our measurements still measure their combined strain and use of different algorithms give consistent results in terms of strain magnitude [52]. Indeed, the cECCI observations here show that slip bands in the solution strengthened and fine-γ' variant are on the order of 30 and 50 nm wide, respectively, the coarse-γ' variant being on the order of 200 nm wide for a single slip band. While a very fine slip trace spacing has been reported for Ni-based superalloys during fatigue by direct imaging techniques [32], this is likely due to slip band irreversibility [53] which is not a consideration for monotonic tension. The discontinuity of a slip band raises an issue of accuracy for measurements of local strain that are an average of locally slipped and

non-slipped material, and investigation of this in the literature is on-going [29,54].

The image correlation results in full-field displacement maps u(x$_1$, x$_2$, 0) on the x$_1 \times$x$_2$ plane with normal x$_3$. The individual components of the displacement gradient tensor can be found by the gradient of the displacement with respect to the macroscopic directions using Eq. (1).

$$\frac{\partial \boldsymbol{u}_i}{\partial \boldsymbol{x}_j} = \begin{bmatrix} \dfrac{\partial \boldsymbol{u}_1}{\partial \boldsymbol{x}_1} & \dfrac{\partial \boldsymbol{u}_2}{\partial \boldsymbol{x}_1} \\ \dfrac{\partial \boldsymbol{u}_1}{\partial \boldsymbol{x}_2} & \dfrac{\partial \boldsymbol{u}_2}{\partial \boldsymbol{x}_2} \end{bmatrix} \tag{1}$$

It is convenient to visualise the local strain by combining the four components of the displacement gradient tensor into an effective strain, ε_{eff} [18]. This is a shear-dominated term, which reflects the characteristic slip, and can be calculated using Eq. (2).

$$\varepsilon_{eff} = \sqrt{0.5\left(\frac{\partial \boldsymbol{u}_1}{\partial \boldsymbol{x}_1} - \frac{\partial \boldsymbol{u}_2}{\partial \boldsymbol{x}_2}\right)^2 + 0.5\left(\frac{\partial \boldsymbol{u}_1}{\partial \boldsymbol{x}_2} + \frac{\partial \boldsymbol{u}_2}{\partial \boldsymbol{x}_1}\right)^2} \tag{2}$$

The positional and displacement data for all alloys are available for download [47–49].

2.5. Data analysis routines

The EBSD data and displacement data were analysed using our own Python NumPy [55] routines and were visualized using Matplotlib [56]. These routines are available through the open source DefDAP library (Deformation Data Analysis in Python) [57]. The manipulation of Euler angles was performed with quaternion algebra, the details for which are well described elsewhere [58–60], and the grain-level misorientation (ϕ) was calculated by the grain reference orientation distribution (GROD Mean) [61], defined as the misorientation of every pixel within a grain with respect to the mean orientation. The EBSD grain boundaries were defined as neighbouring pixels with a misorientation greater than 5° The boundaries were used to masque grains for both the EBSD and the HRDIC data. The EBSD grain boundaries were mapped onto the HRDIC data using manually selected homologous material points (usually triple junctions that are obvious in both data sets) to define an affine transform (resize, shear, rotation) between the two datasets. The affine transformation accounts for the distortion associated with specimen tilting [62,63] but cannot account for distortions that arise from barrelling effects at low magnification nor distortions due to drift [63]. Therefore, we have taken multiple smaller EBSD maps at higher magnification as recommended by Nolze [62] and use a piecewise affine transformation to account for any drift, although none was immediately evident. While alternative methods have been proposed for better fit of EBSD data to data obtained at zero tilt [63,64], we find the affine approach works well for the distortions encountered on our microscope. This procedure then enables grain segmentation of the HRDIC data and single grain analysis of plastic strain for several hundreds of grains, as does its correlation to lattice misorientation data from EBSD.

2.6. Single grain analysis of slip character

Single grains are isolated from the HRDIC data using manually selected homologous material points (usually triple points that are obvious in both data sets) to define an affine transform (resize, shear, rotation) of the EBSD grain boundaries onto the HRDIC strain data.

The following slip characteristics are quantified for each grain: number of slip planes, slip planarity (planar, diffuse or a mixture of the two), the presence of cross slip, slip band bifurcation, slip band fading towards a grain boundary and slip band impingement upon a grain boundary. As the analysis could be not be easily automated the analysis was performed manually for ~ 500 grains in each alloy variant. The number of slip systems was determined as the number of

non co-planar slip plane families within the grain. The slip planarity was characterised as either planar or diffuse: planar slip is characterised by well-defined, lamella slip and diffuse slip was characterised by strain above the uncertainty in the strain measurement (0.01) and but, if planar, then very fine slip that creates diffuse regions of strain. If a grain contained less than ~10% diffuse strain, as measured by eye, it was categorised as a grain exhibiting planar slip and, likewise, if a grain contained less than ~10% planar slip it was categorised as exhibiting diffuse slip. Grains with a mixture of the two types of slip contained both planar and diffuse characteristics outside of this 90:10 split. The presence of other slip characteristics, such as cross slip, slip band bifurcation, fading and impingement were counted if any such instance occurred within a grain. Note that a single grain may contain many or even all of these additional characteristics.

2.7. Image analysis

To quantify the amounts of well-defined planar slip and diffuse high-strain regions, band width filters were applied to the DIC images. Low frequencies correspond to diffuse hot spot regions while high frequencies correspond to sharp and high frequency slip traces. The filter parameters were optimised for the solid solution alloy because this alloy contains the most homogeneous strain distribution and is therefore the most sensitive to thresholding. The same masque and threshold parameters principles were then applied to the strain maps of the other two alloys. The FFT was masked with a circular region of interest with a diameter equal to 5% of the pixel size of the FFT. The inverse FFTs were thresholded to half the maximum height of the intensity frequency distribution. We found that this provided sufficient detail to capture the slip traces and the diffuse strain regions.

2.8. Electron channelling contrast imaging

Diffraction-controlled cECCI allows the site-specific imaging of defects; recent work has demonstrated its usefulness in identification of slip band interactions with microstructural features [32,65]. The interested reader is directed elsewhere for a detailed review on the ECCI method [46]. In the present work, cECCI was applied to further investigate plastic strain and lattice distortion in areas selected from HRDIC and EBSD measurements, respectively. This approach avoided the use of much more time consuming and volume-limited TEM investigation. Here, a Zeiss Sigma FEG-SEM with a Gemini column was used for its highly parallel beam at an accelerating voltage of 30 kV. An aperture size of 120 μm in high current mode resulted in a high probe current of ~12 nA. Imaging was performed using a retractable 16 mm circular backscatter electron (BSE) detector made by Deben. High current is necessary to reduce noise of the relatively weak channelling signal. Despite this relatively high current, the lateral resolution of the image stays in the order of 10 nm, which is sufficient to resolve the here appearing dislocation densities. A Kleindiek E5AT eucentric substage with precise sample tilt and rotation axes was used to position the sample in accurate well-defined channelling conditions. The tilt and rotation angles for well-defined channelling conditions were determined by measuring the crystal orientations with EBSD and then applying the software TOCA to simulate the electron channelling patterns for different stage positions. The relative positions of stage and EBSD detector was calibrated using a single crystal Si ⟨100⟩ using a procedure outlined in [46]. Electron channelling contrast follows the same principles as diffraction imaging in TEM: in order to image an area by excitation of a certain diffraction vector, $\mathbf{g}_{(hkl)}$, the lattice planes (hkl) need to be tilted such that the primary electron beam impinges on these planes under the Bragg angle θ(hkl). In a Kikuchi pattern this corresponds to the case that the primary beam direction is on one of the (hkl) Kikuchi lines (this case is called the "two-beam" case in TEM). Under these conditions the electrons channel deep into the lattice and produce very

few backscattered electrons. In a BSEI the area under observation thus appears dark. Extended defects that distort the lattice planes (hkl) disturb the electron channelling and lead to strong backscattering. As a consequence these defects are visible by high intensity on an otherwise dark background. In the Ni-based material investigated here the defect contrast is observable up to a depth of about 80 nm below the surface [46], which is similar to the thickness of conventional TEM thin foils.

As the (111) planes are giving the strongest electron channelling contrast we used exclusively (111) diffraction vectors. Furthermore, as the (111) planes are the common glide planes in superalloys all ECC images displayed in this work will show all (111) traces at the bottom of the images. The blue line corresponds to the (111), the green line the ($\bar{1}$11), the yellow the (1$\bar{1}$1) and the red line the (11$\bar{1}$). The lengths of the slip traces in the legend are proportional to the angle between the slip plane normal for that slip trace and the sample surface normal. The longest line is always at almost 90° to the surface normal and corresponds to the plane that is used for imaging.

3. Results

3.1. Material characterisation

The heat treatments [14] produced two different precipitation-strengthened alloy variants. The fine-γ' variant contained a bimodal distribution of intragranular precipitates with sizes of 70 ± 22 nm diameter secondary γ' (volume fraction~0.3) and 10 nm diameter tertiary γ' (volume fraction ~0.1). The coarse-γ' variant contained a unimodal distribution of intragranular precipitates with sizes of 250 ± 75 nm diameter γ' (volume fraction ~0.4). The size variation given corresponds to a single standard deviation from the mean. Example images of the secondary precipitates can be seen in the supplementary material, together with their size distributions. All γ' precipitates were spheroidal and previous work has shown that the γ/γ' lattice misfit for the RR1000 microstructures is very low [12]. The γ phase grain diameter was obtained from EBSD data as the equivalent circle of the grain area. In the fine-γ' variant the mean grain diameter is ~15 μm, for the coarse-γ' variant it is ~16 μm and for the solution-strengthened alloy it is ~9 μm. Texture analysis of EBSD data showed no strong texture in any of the three alloys studied; the (100), (110) and (111) pole figures are available in the supplementary material. The fraction of grain boundaries that are Σ3 recrystallisation twins is equal to 49% for the fine- γ' variant, 46% for the coarse-γ' variant and 51% for the solid solution alloy.

3.2. Macroscopic deformation response

Fig. 1(a) shows the true stress − true strain (σ_T - ε_T) flow curve under monotonic tension to fracture for all three alloy variants. Fig. 1 (b) shows the strain-hardening (dσ_T/dε_T) plotted against ε_T. Fig. 1(a) and (b) both contain a grey dotted line that accounts for the elastic relaxation on unloading to indicate the 2% macroscopic plastic strain at which all of the microstructure investigations were carried out. The yield strength of the precipitation- strengthened alloys is four times larger than that of the solution-strengthened alloy; the yield strength of the fine-γ' variant is slightly larger than the coarse-γ' variant (factor 1.07 larger). Compared to the precipitation-strengthened alloys, the solution-strengthened alloy shows twice larger elongation to fracture. The precipitation-strengthened alloys both show greater early stage strain hardening than the solution-strengthened alloy and the coarse-γ' variant more than the fine-γ' variant. While the solution-strengthened alloy shows a monotonic decay in the strain hardening, both precipitation-strengthened alloys show an increase in strain hardening at a plastic strain of ~2% (total strain of ~3%).

Table 2 details the modulus of elasticity (E), the 0.2% proof stress to indicate plastic yield ($\sigma_{Y0.2}$), the ultimate tensile stress (σ_{UTS}), the
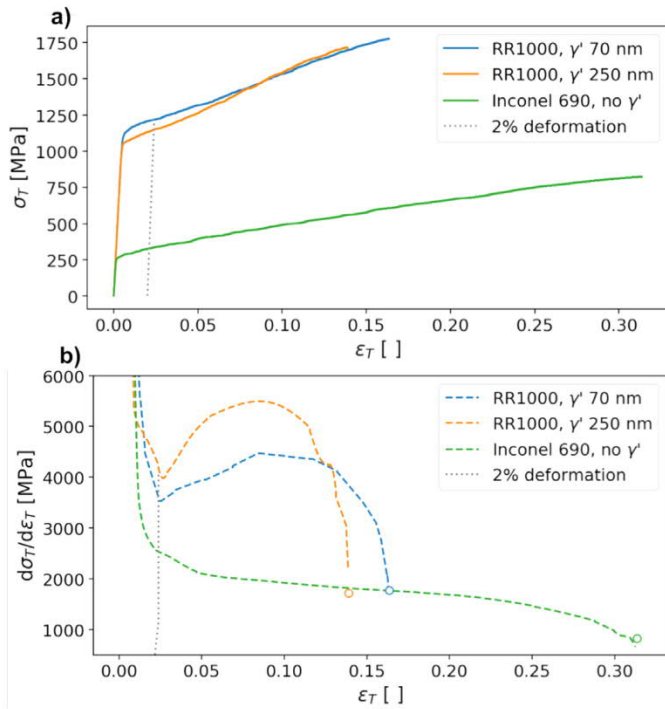
a)

b)

Fig. 1. The a) true stress and b) strain-hardening flow curves to failure as a function of true strain for the fine-γ' variant, the coarse- γ' variant and the solid solution alloy. (For interpretation of the references to colour in this figure legend, the reader is referred to the web version of this article.)

total magnitude of strain-hardening ($\sigma_{SH} = \sigma_{UTS} - \sigma_{Y0.2}$), the magnitude of the strain-hardening as a fraction of the yield ($\sigma_{SH}' = \sigma_{UTS} / \sigma_{Y0.2}$), and the total elongation (ε_T). Most of the values measured match those expected, with the exception of E of Inconel 690 at 170 GPa, which is much lower than expected (211 GPa). This disparity is probably due to micro-yielding happening at very low applied stresses, contributing to the apparent measured elastic strain.

3.3. Deformation patterns analysis

For microstructure analysis specimens of all three alloy variants were deformed under uniaxial tension to a macroscopic axial strain of ~2%, although the absolute macroscopic strain will differ slightly between specimens. This amount of deformation captures the onset of plasticity and the beginning of the increase in strain hardening for the precipitation-strengthened alloys, and is beyond the magnitudes relevant to low cycle fatigue. Fig. 2 shows the effective shear strain (ε_{eff}) map obtained from the HRDIC strain data for all three alloys. On average ε_{eff}~0.02, but locally ε_{eff} values can be as low as 0.00 or as high as 0.50. As all of the data is presented on the same ε_{eff} (colour) scale, it is clear that the strain localisation is greater in the γ'-strengthened alloys compared to solution-strengthened alloy, the former of which contain fewer slip traces with a larger slip trace spacing and highly localised shear with greater strain magnitude. In the solution-strengthened Inconel 690 there are more slip traces with lower strain intensity and the magnitude of strain between the traces is higher in the solution-strengthened alloy compared to the precipitate-strengthened alloys. Because of the finite lateral resolution, it is not possible to distinguish whether the

higher strain between slip bands is due to the presence of very fine, closely spaced slip bands, or due to non-planar slip. In either case, the deformation corresponds to slip; it is our measure the slip characteristics it that we can quantify.

The deformation at the scale of the maps in Fig. 2 contains microscopic and mesoscopic features. On the microscopic scale there are planar, high frequency slip domains within single grains, measured to be orientated (mean) $\pm$ ~50° (range $\pm$ 25 − 63 °) to the tensile axis. The slip in these discrete regions most often occurs on the {111} planes most favourably orientated for slip in agreement with the highest Schmid factor. At the mesoscopic scale, there are diffuse strain hotspots observed in the strain maps for all three alloy variants. The diffuse regions link together between neighbouring grains and often concentrate at grain boundaries and triple junctions. As noted above, these regions may be diffuse strain (on multiple slip systems) or they may be very fine slip that cannot be resolved with the method employed here. However, they represent a measurably different type of deformation. The diffuse regions form long-range bands-like features through the microstructure at the mesoscale and therefore cannot be predicted from local neighbourhood deformation incompatibilities alone. At grain boundaries, the diffuse strain magnitude is increased and seems to be associated with local impingement of slip bands on the grain boundaries, which suggests they are created because of poor slip transfer between direct grain neighbours. These mesoscopic deformation bands have been shown in single crystals [66] and in polycrystals [67] to be non-crystallographic and, as shown here, are measured to be orientated (mean) $\pm$ ~53° (range $\pm$ 40 − 60°) to the tensile axis.

Fig. 3 shows the GROD Mean misorientation data for the same field of view as the strain maps in Fig. 2. Like the strain data, there are misorientation hotspots that are spatially associated with the mesoscopic diffuse-strain deformation bands in Fig. 2. The relationship between misorientation and strain is discussed in detail elsewhere [68] for the coarse-γ' variant.

In order to quantify the levels of strain heterogeneity we define the normalised effective strain, $\langle \varepsilon_{eff} \rangle$, which divides each strain value (ε_{eff}) by the map mean $\overline{\varepsilon_{eff}}$.

$$\langle \varepsilon_{eff} \rangle = \varepsilon_{eff} \overline{\varepsilon_{eff}} \tag{3}$$

and we calculate the normalised misorientation, $\langle \phi \rangle$, in the same way. Fig. 4 shows that the $\langle \varepsilon_{eff} \rangle$ distributions in the fine-γ' variant is more heterogeneous than the coarse-γ' while the $\langle \varepsilon_{eff} \rangle$ distributions in the solution-strengthened alloy suggest far more homogeneous strain (almost normal distribution of values with the mode close to the mean). The variation in plastic strain localisation between the three alloys is therefore not reflected in the lattice misorientation data, which is because of the scaling property of lattice misorientation data, a phenomenon that is well known but not well understood [69]. The absence of this scaling in plastic strain indicates a fundamental difference in the two measures of deformation: EBSD only measures residual plastic strain and the lattice rotations that arise due to incompatibility between neighbouring regions of opposed plastic strain and the requirement to preserve a continuum [26].

Damage accumulation in plastic strain hotspots is thought to be important for localised failure mechanisms [70−72]. The diffuse strain regions in the maps of Fig. 2 might correspond to such hotspots. A band pass filter was applied to the Fast Fourier Transform

Table 2
Mechanical properties derived for the alloy variants in this work.

Alloy	E [GPa]	$\sigma_{Y0.2}$ [MPa]	σ_{UTS} [MPa]	σ_{SH} [MPa]	σ_{SH}' [MPa]	ε_T []
RR1000, γ' 70 nm	222	1130	1770	640	1.57	0.140
RR1000, γ' 250 nm	215	1060	1720	660	1.62	0.118
Inconel 690, no γ'	170	270	820	550	3.04	0.310
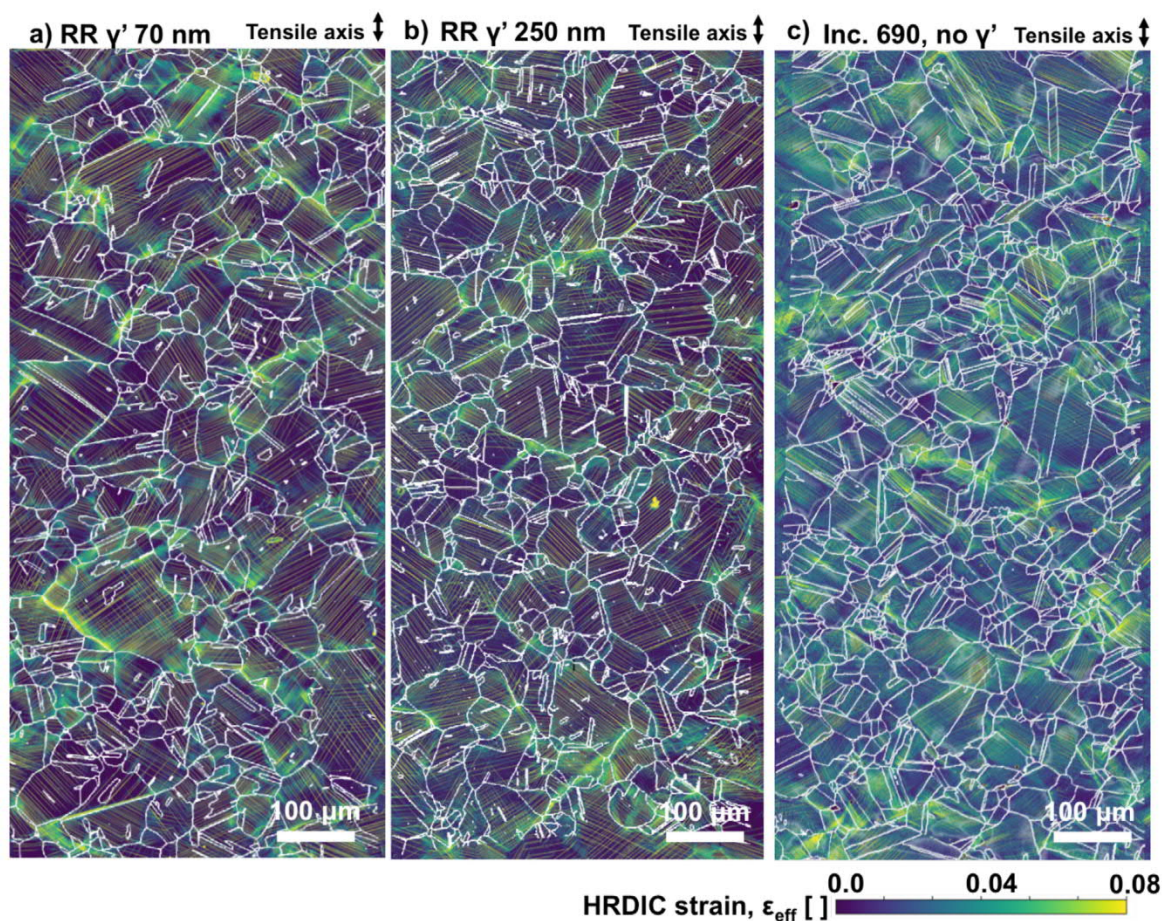
Fig. 2. The HRDIC effective strain (ε_{eff}) maps for a) the fine-γ' variant, b) the coarse- γ' variant and c) the solid solution alloy. The tensile axis is vertical and all maps are plotted on the same colour scale. The field of view is 1×0.5 mm and the spatial resolution 117 nm.

(FFT) of the strain maps to separate data related to sharp slip (outer part of the FFT) and diffuse slip (inner part of the FFT). Fig. 5 shows the overlaid maps of sharp slip and diffuse slip and the associated FFTs for the original strain maps as inserts for each of the three alloy variants. From this, the area fractions of sharp slip and diffuse slip were calculated. The fine-γ' variant contains 12% sharp slip and 11% diffuse slip, the coarse-γ' variant contains 13% sharp slip and 9% diffuse slip and the solid solution alloys contains 23% sharp slip and 8% diffuse slip. The diffuse regions can be compared to the regions of high lattice misorientation to show that the two phenomena are not, in fact, spatially coincident. However, there certainly is a spatial relationship between them. It is therefore likely that the misorientation hotspots are closely associated with the gradient of the diffuse strain hotpots [68].

A study of the FFTs themselves can tell us something about slip character because the periodic angular relationships in the real-space maps are preserved in the FFTs. The FFT for the fine-γ' alloy in Fig. 5 part a) shows more sharp signals in the mid-frequency range, whereas the coarse-γ' alloy in part b) and especially the solution-strengthened alloy in part c) show more diffuse signals in this region. This indicates that the slip is sharper and more well defined in the fine-γ' alloy. In the high frequency range, the fine-γ' alloy shows no signal whereas the coarse-γ' and solution-strengthened alloy show signals at $\pm 90°$ Signals at these positions indicate neighbouring pixels at 90° to one another that have the same strain value. In real space the majority of slip bands are orientated $\pm 25-63°$ to the loading direction. Therefore, high frequency signals in the FFT at $\pm 45°$ or $\pm 90°$ are indicative of slip trace width. From Fig. 5b) we can therefore conclude that the slip traces in the coarse-γ' variant are wider than those in the fine-γ' variant. Further, there is greater

intensity in the $\pm 45°$ high frequency domain for the coarse-γ' than the solution-strengthened alloy, indicating that the slip traces in the coarse-γ' alloy are wider than those in the solution-strengthened alloy. The $\pm 90°$ intensity in the solution-strengthened alloy FFT contains more detail than that in the coarse-γ' alloy, indicating many close parallel slip traces in the Inconel 690 as opposed to wider slip traces.

To investigate the reason for variable slip trace morphologies and levels of strain localisation, the defects within slip bands were characterised directly by cECCI. Fig. 6 shows this analysis for the fine-γ' and coarse-γ' variants at the same magnification using the $\boldsymbol{g} = \overline{1}11$ diffraction vector, highlighting slip bands (denoted SB in the figure) and stacking faults (denoted SF in the figure). The SFs are present in the fine-γ' variant before deformation and are therefore likely to have been introduce during the heat treatments. In the coarse-γ' variant, the linear features are all slip bands and no stacking faults are observed. The slip bands in the investigated grain from the fine-γ' variant are parallel to (yellow) $(1\overline{1}1)$, which are tilted away from the edge-on condition by 19.0° For the grain selected from the coarse-γ' variant two slip traces are observed: those parallel to (yellow) $(1\overline{1}1)$ are 28.5° from the edge-on orientation and those parallel to (green) $(\overline{1}11)$ are 18.1° from the edge-on condition. As the (yellow) $(1\overline{1}1)$ slip bands in the grain from the fine-γ' variant and the (green) $(\overline{1}11)$ slip bands in the grain from the coarse-γ' variant are tilted off-normal to a similar magnitude their projected widths can be compared directly. It is found that the wider slip traces in the coarse-γ' variant are due to wider underlying slip bands. Fig. 6(d) shows that the width of the slip bands in the coarse-γ' variant is related to the size of the γ' precipitates and that multiple parallel active glide planes are necessary to overcome them. The mechanism for this generation of wider
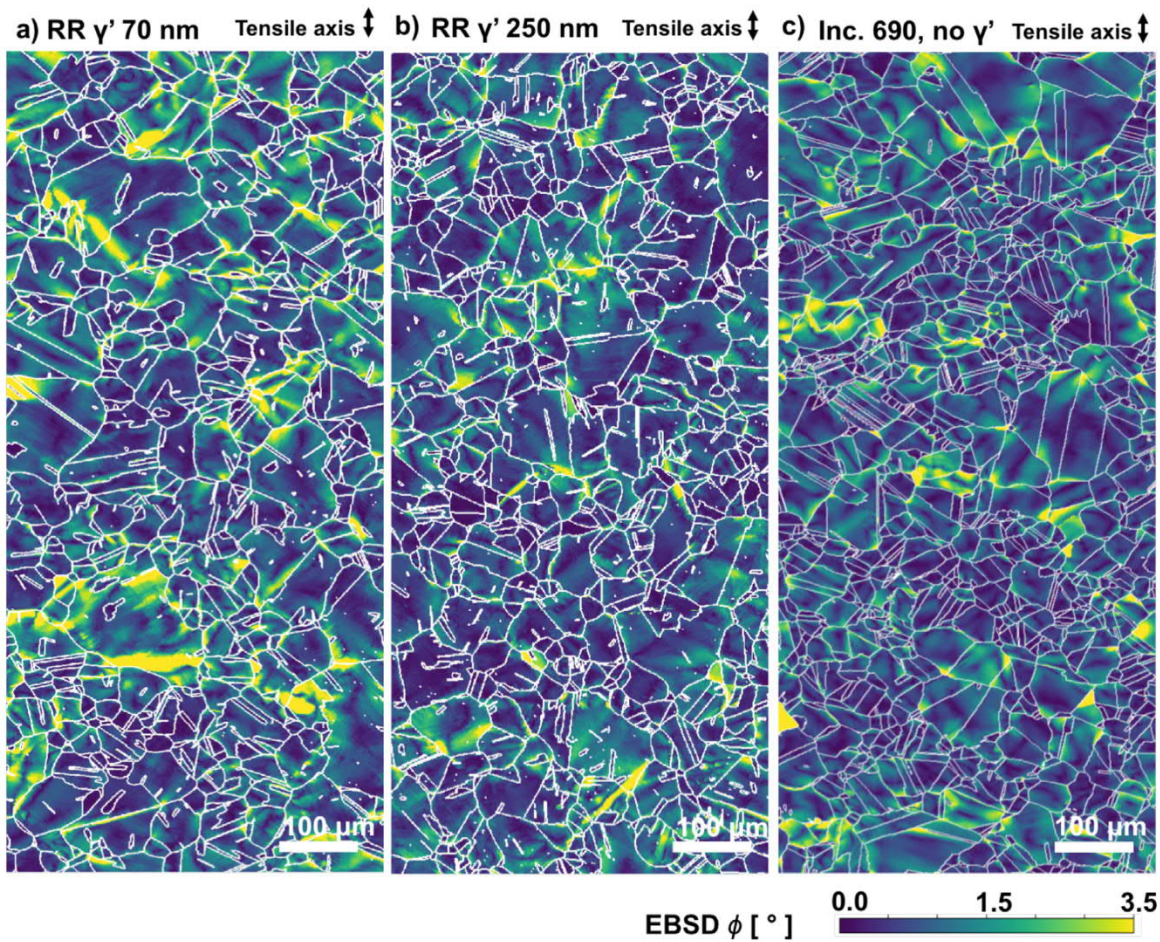
Fig. 3. The EBSD misorientation maps for a) the fine-γ' variant, b) the coarse- γ' variant and c) the solid solution alloy. The tensile axis is vertical and all maps are plotted on the same colour scale. The field of view is 1×0.5 mm and the spatial resolution 500 nm.

slip bands is likely Orowan looping and local cross slip to overcome obstacles [73].

3.4. Grain specific deformation character

Representative examples of sub-grain deformation character within individual grains are shown in Fig. 7, Fig. 8 and Fig. 9 for the fine-γ' variant, the coarse-γ' variant and the solution-strengthened alloy, respectively. In many cases, the spatial location of the misorientation ϕ reflects a change in the gradient of the ε_{eff}, but this is not always the case, especially for complex slip morphologies. For the fine-γ' variant the most common slip characteristics are planar slip, slip band bifurcation (especially towards grain boundaries), very finely spaced slip (often multi-slip), fading of slip bands towards grain boundaries and the impingement of slip bands on grain boundaries, the latter causing significant strain localisation and lattice distortion. For the coarse-γ' variant some of the deformation characteristics from the fine-γ' variant are also observed, such as planar slip, slip band bifurcation and slip band impingement. However, the coarse-γ' variant also exhibits cross slip and diffuse slip characteristics, which are rarely observed in the fine-γ' variant. Finely spaced slip, sometimes observed in fine-γ' variant, is never observed in the alloy with larger γ'. The solution-strengthened alloy shows much less localised strain, finer spaced and more diffuse slip, with some instances of cross slip but not many, and no instances of slip band bifurcation at all. There are some instances of slip band impingement on grain boundaries, but more often the slip bands will fade as they approach grain boundaries.
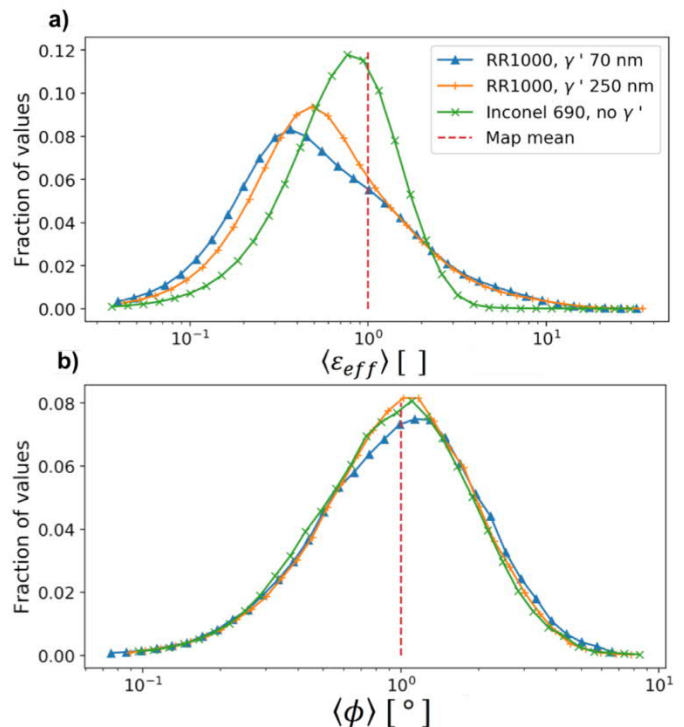
Fig. 4. The distribution of normalised a) HRDIC strain $\langle \varepsilon_{eff} \rangle$ and b) EBSD misorientation $\langle \phi \rangle$ relative to the map means.
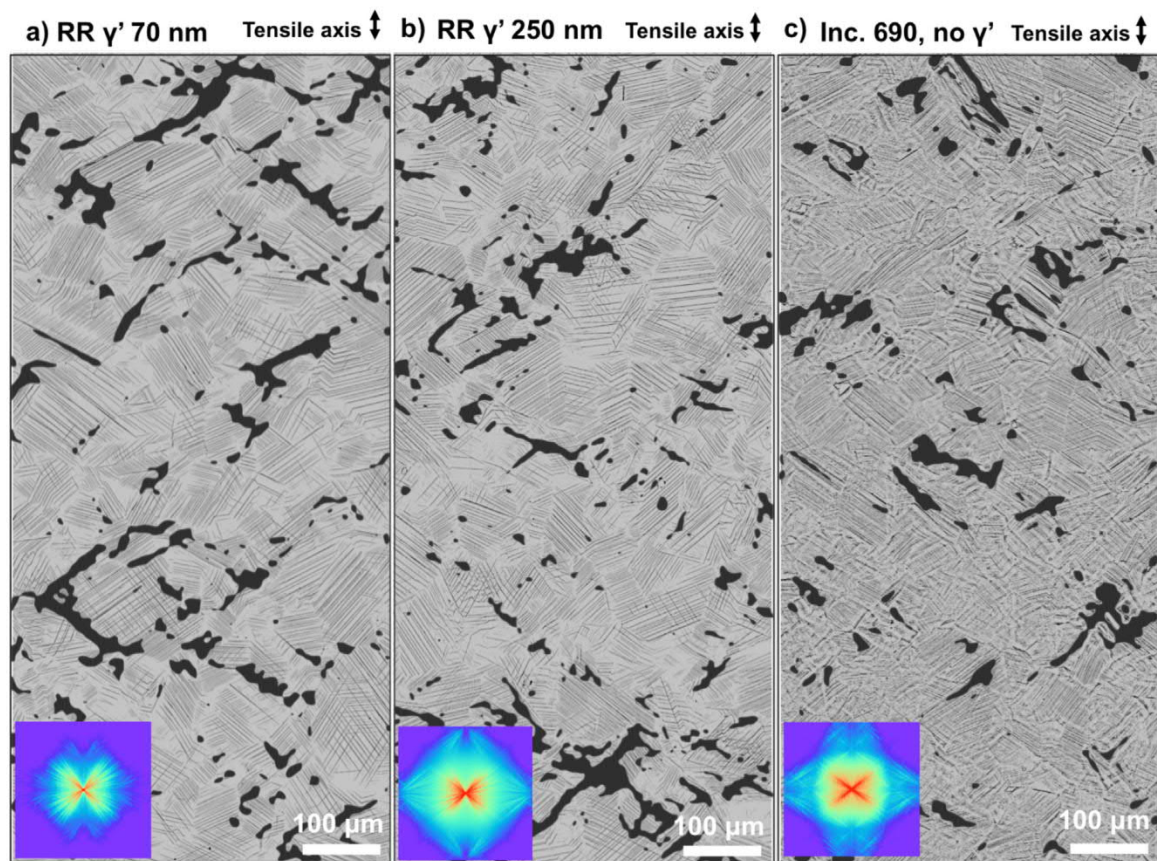
Fig. 5. The overlaid low and high frequency inverse FFT maps for a) the fine-γ' variant, b) the coarse- γ' variant and c) the solid solution alloy highlight sharp and diffuse slip characteristics. Both high and low frequency slip is displayed in black. Low magnitude strain is displayed in grey. The inserts show the FFTs, plotted on the same 8-bit scale with a rainbow colour theme to highlight details.
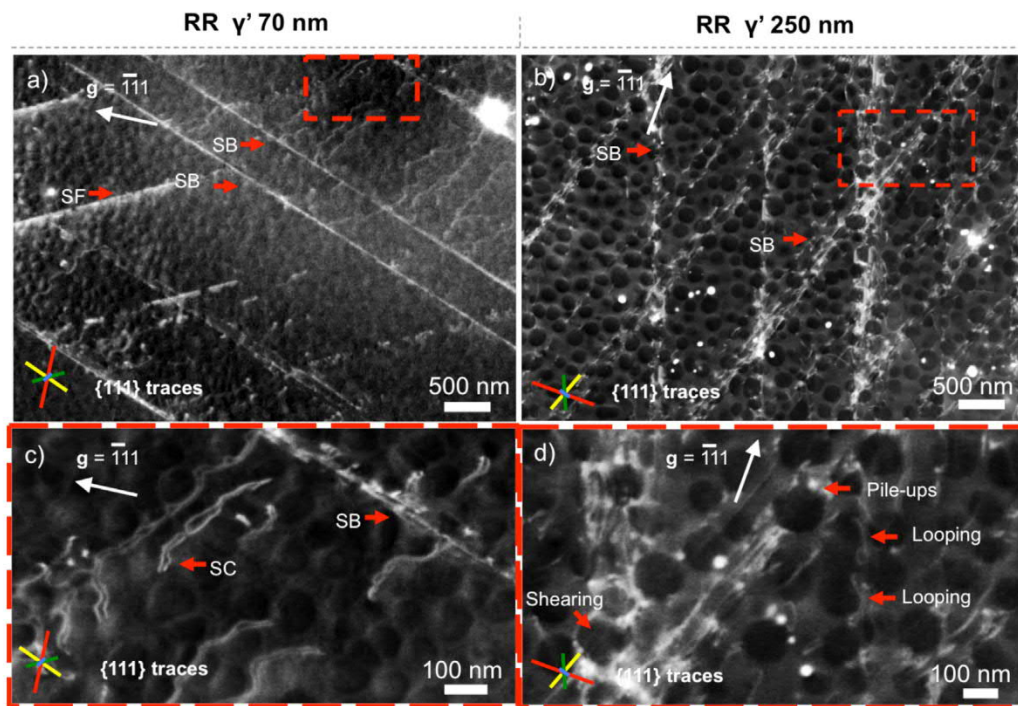

Fig. 6. ECCI analysis to determine slip band widths and dislocation-γ' interactions for the fine-γ' variant (left) and the coarse- γ' variant (right) using the $g = \overline{1}\overline{1}1$ diffracting vector. The red dotted boxed in parts a) and b) are magnified in parts c) and d), respectively. The {111} slip traces are shown for each image as four coloured lines, the length of the line representing the angular distance between the plane normal and the sample normal. Key: SB = slip band; SF = stacking fault; SC = strongly coupled dislocations. (For interpretation of the references to colour in this figure legend, the reader is referred to the web version of this article.)
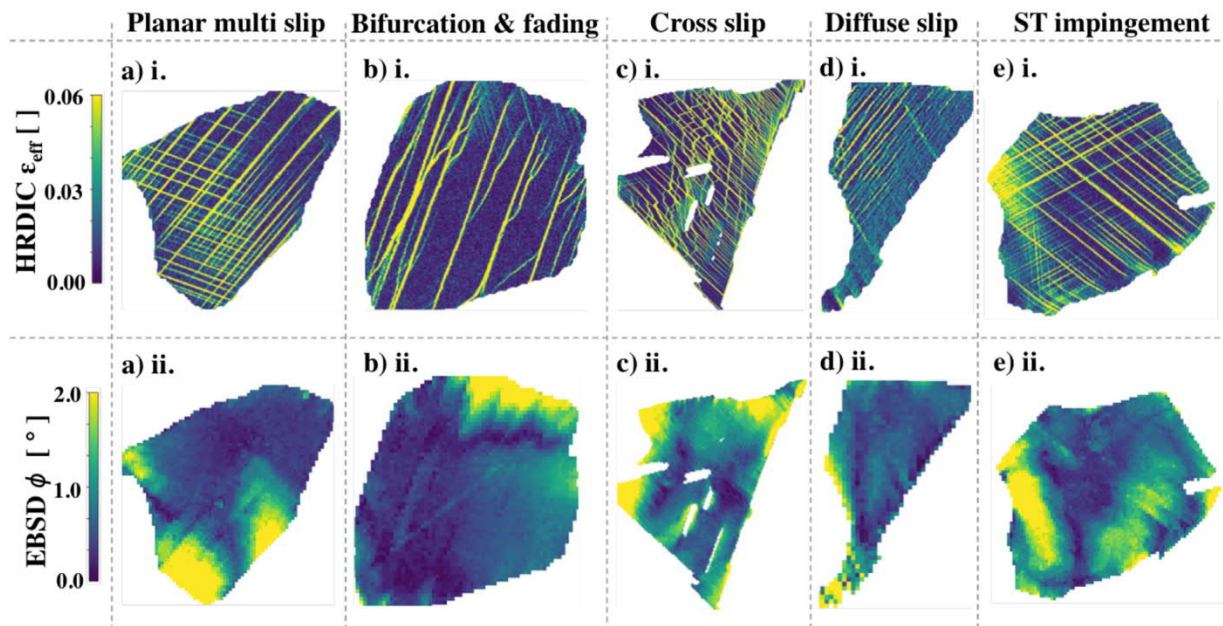
Fine-γ' variant
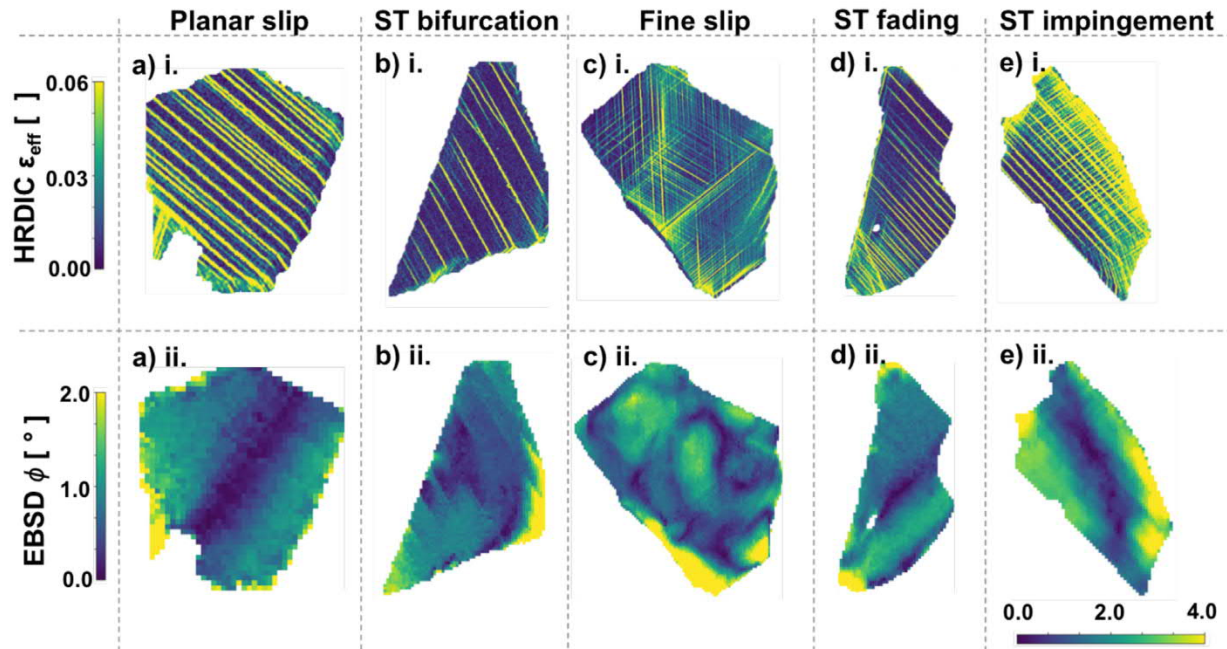
Fig. 7. Representative examples of grains with different slip characteristics are shown for the fine-γ' variant: a) planar, well-defined slip, b) slip band bifurcation, c) very fine planar slip, d) slip band fading and e) slip band impingement, causing strain concentration close to the grain boundary. In parts i. we show the HRDIC strain data and in parts ii. the EBSD misorientation data.

Utilising again Eq. (3) but now for individual grains the heterogeneity of strain within a grain can be numerically characterised by the gradient of the tail in its distribution of $\langle \varepsilon_{eff} \rangle$ In this analysis shallow gradients ($slope \rightarrow 0$) indicate wide variation in the strain values relative to the mean and therefore strain heterogeneity, whereas sharp gradients ($slope \rightarrow -\infty$) indicate a small variation of strain values relative to the mean and therefore strain homogeneity within a grain. We call this the strain distribution gradient and an outline of the procedure for its calculation is provided in the supplementary material. The strain distribution gradient has been calculated for 471 grains in the fine-γ' variant, 613 grains in the coarse-γ' variant and 566 grains in the solution-strengthened alloy and is plotted against the mean grain strain in Fig. 10. The correlation between mean grain ε_{eff} and misorientation ϕ is shown by the

Coarse-γ' variant

Fig. 8. Representative examples of grains with different slip characteristics are shown for the fine-γ' variant: a) planar, well-defined multi-slip, b) slip band bifurcation and fading, c) cross-slip, d) diffuse slip and e) slip band impingement, causing strain concentration close to the grain boundary. Parts i. show the HRDIC effective strain data and parts ii. show the EBSD misorientation data.
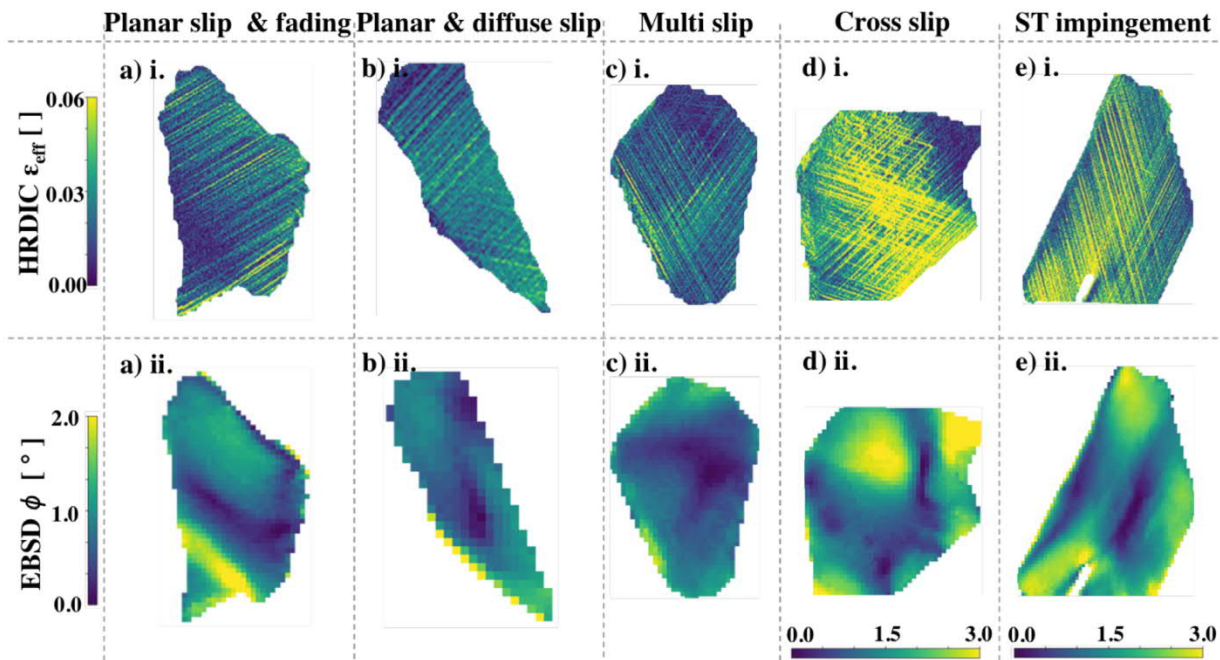
Fig. 9. Representative examples of grains with different slip characteristics are shown for the solution-strengthened alloy: a) planar slip and slip band fading, b) slip that is planar in a part of the grain and diffuse in another, c) planar multi-slip, d) cross-slip and e) slip band impingement, causing strain concentration close to the grain boundary. Parts i. show the HRDIC strain data and parts ii. show the EBSD misorientation data.

change in colour from blue to yellow with increasing ε_{eff}. There is a wide distribution in grain mean strain and grain strain heterogeneity. Importantly, as the mean grain strain increases, the grains in the precipitation-strengthened alloys become more heterogeneous whereas the grains in the solution-strengthened alloys become more homogeneous.

The representative examples of sub-grain deformation characteristics show significant differences in the spatial distribution between the slip and the lattice misorientation. In most cases, the misorientation is located close to a grain boundary but the majority of the slip is not. Fig. 11 shows a frequency distribution of the average distance within grains between the upper quartile of strain or misorientation values and the nearest grain boundary for 406 grains in the fine-γ' variant, 549 grains in the coarse-γ' variant and 531 grains in the solution-strengthened alloy. The distance is the fractional distance to the grain centre, so a distance of 0 is at the boundary and a distance of 1 is at the grain centre. The figure also plots the frequency distribution

of a random distribution of values within the grain. The highest strain values show no affinity for any spatial region of the grain, i.e. not towards the boundary nor the centre. However, the greatest misorientation values within a grain show a strong affinity for grain boundaries and even more so in the precipitation-strengthened alloys than in the solution-strengthened alloy. It is important to note that the misorientation is physically closer to the boundaries in the solid solution alloy ($< \sim 3$ um from the boundary) compared to the precipitation-strengthened alloys ($< \sim 5$ um), but this does not account for the variation in grain size; when we normalise for grain size the trend is reversed. This indicates greater misorientation heterogeneity in the precipitate-strengthened alloy grains and that misorientation is more strongly associated with their boundaries.

The slip characteristics in Figs. 7, 8 and 9 describe the number of slip trace families in a deformed grain, the slip planarity and the mechanisms employed to accommodate local deformation incompatibilities: cross-slip, slip trace bifurcation, fading towards a grain boundary and
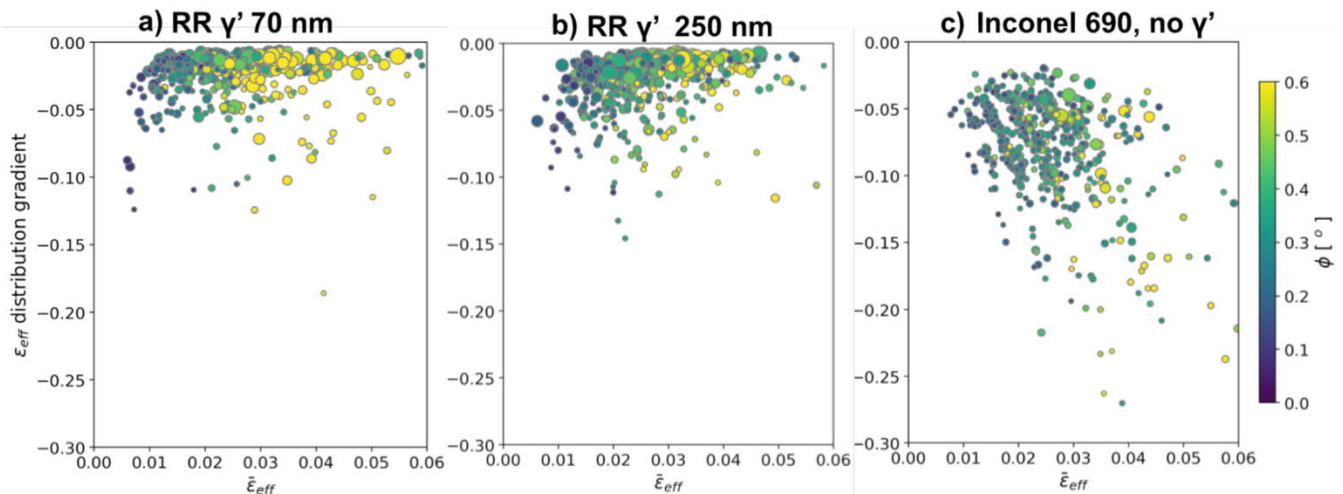

Fig. 10. The variation in sub-grain strain heterogeneity as a function of mean grain strain for a) the fine-γ' variant, b) the coarse-γ' variant and c) the solid solution alloy. *gradient* $\to 0$ indicates strain heterogeneity and *gradient* $\to -\infty$ indicates strain homogeneity. The colour and size of the data point relate to the grain average EBSD misorientation.
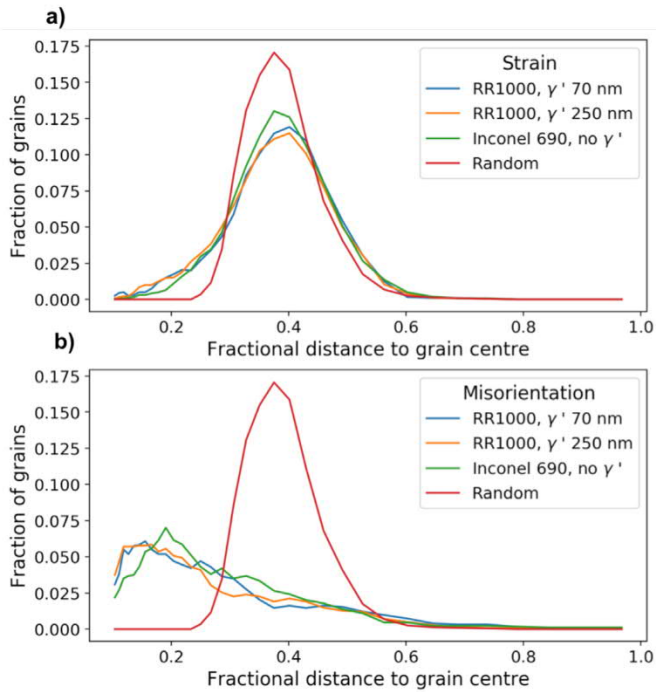
Fig. 11. The average distance to the nearest grain boundary for the upper quartile of a) strain and b) misorientation values within a grain, plotted as a frequency distribution for all grains in the fine-γ' variant, the coarse- γ' variant and the solid solution alloy. (For interpretation of the references to colour in this figure legend, the reader is referred to the web version of this article.)

Fig. 12. An analysis of the slip character in each of the three alloys by the fraction of grains that contain that character. Part a) details the number of slip systems, part b) details the slip planarity and part c) details the mechanisms used to accommodate local deformation incompatibilities: cross-slip, slip trace bifurcation, slip trace fading and slip trace impingement. (For interpretation of the references to colour in this figure legend, the reader is referred to the web version of this article.)

impingement upon it. The occurrence of these characteristics have been counted in 660 grains for the fine-γ' variant, 785 grains for the coarse-γ' variant and 1061 grains for the solid solution alloy. Fig. 12 contains a series of bar charts to show the fraction of grains that contain these characteristics. It should be noted for part c) that if a grain contains more than one characteristic then it is counted twice, so the measure is the fraction of grains that contain at least one example of the characteristic. Whilst this slip trace analysis did not include the relevant crystallographic data, all grains in which a full slip trace analysis has been performed (32 grains) have indicated slip on {111} planes only. The occurrence of only {111} slip is supported by the maximum number of non co-planar slip traces in Fig. 12a) being equal to 4.

The solution-strengthened alloy has the largest fraction (~0.1) of grains with no slip traces, indicating diffuse deformation or no deformation at all, followed by the coarse-γ' variant and then the fine-γ' variant. Similarly, the solution-strengthened alloy has the highest fraction of grains with only a single slip trace operating at a fraction ~0.38 of grains, followed by the coarse-γ' variant and then fine-γ' variant. For grains in which there are multiple slip systems (2, 3 or 4 non co-planar slip traces), this trend is reversed; the fine-γ' variant has the greatest fraction of grains with multi-planar slip, followed by the coarse-γ' variant and finally by the solution-strengthened alloy.

The slip has been defined as either planar, diffuse, or a mixture of the two in different parts of the grain, as in Fig. 8(d). This diffuse slip is different to that described in Fig. 5 as diffuse slip was there identified as that with a reasonably high magnitude of strain; here the magnitude is not considered. Fig. 12(b) shows that the slip in the fine-γ' variant has more planar character and the solution-strengthened alloy has more diffuse character, with the coarse-γ' variant in between. Fig. 12(c) shows that the coarse-γ' variant has the greatest amount of cross slip and bifurcation occurring, followed by the fine-γ' variant, and with very little of this character in the solution-strengthened alloy, suggesting that exotic slip characteristics are necessary to overcome precipitates. The main slip characteristics for the solution-strengthened alloy are slip band fading and slip band impingement on grain boundaries, but the
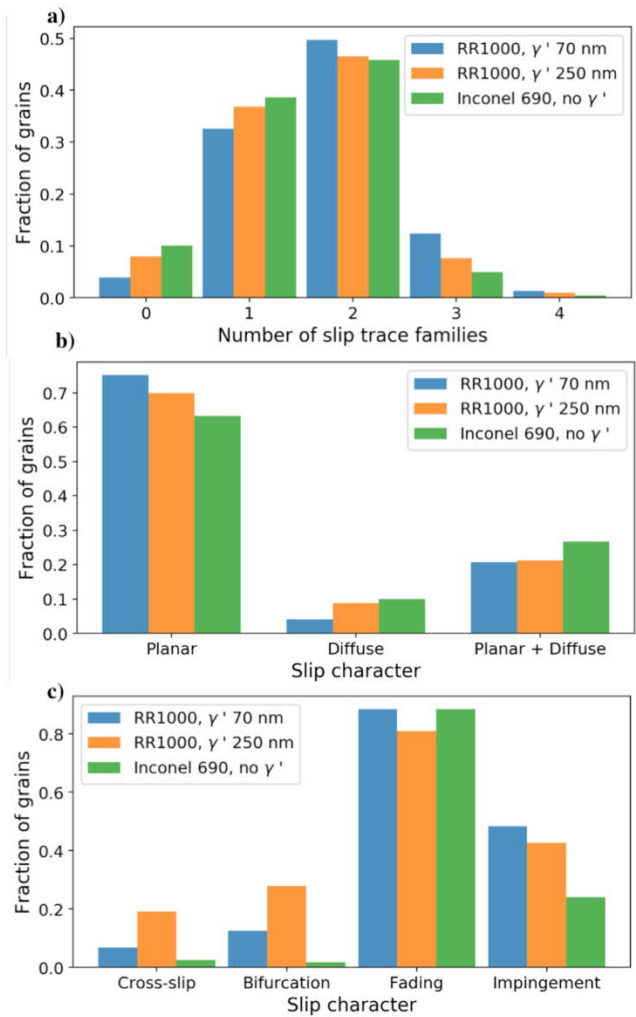
fine-γ' variant displays the most impingement phenomena, followed by the coarse-γ' variant.

Grain orientation predictors of deformation, such as the Schmid factor or Taylor factor are often used to understand local deformation [74–78], although the magnitude of local strain is only very weakly dependant on such parameters [68],. The variation of the Schmid and Taylor factor with orientation are shown in the supplementary material. To assess the effect of grain orientation on the deformation character, Fig. 13 plots the data in the bar charts of Fig. 12 on inverse pole figures (IPFs) from the loading direction. The slip characteristic data for the IPFs have been given a value of 1 for 'present' and 0 for 'absent' so that the scatter plots can be smoothed by linear interpolation for easier observation of trends. While there is no correlation to grain orientation for most of the deformation characteristics, the occurrence of cross-slip and slip band bifurcation seem to be more prevalent in grains that have their orientation in the loading direction parallel to ⟨111⟩. While these grains are those with a high Taylor factor (> 3.) and a low Schmid factor (< 0.35), we propose that this is coincidental. In reality, <111> plans have fewer total active slip systems than <100> but for <111> grains all slip directions are active, two on each of three slip planes. Therefore, all slip directions can occur on three planes, whereas for <111> grains only two slip directions are active, albeit on all four planes. In the solution-strengthened alloy the cross slip is at the atomic scale and so we do not observe
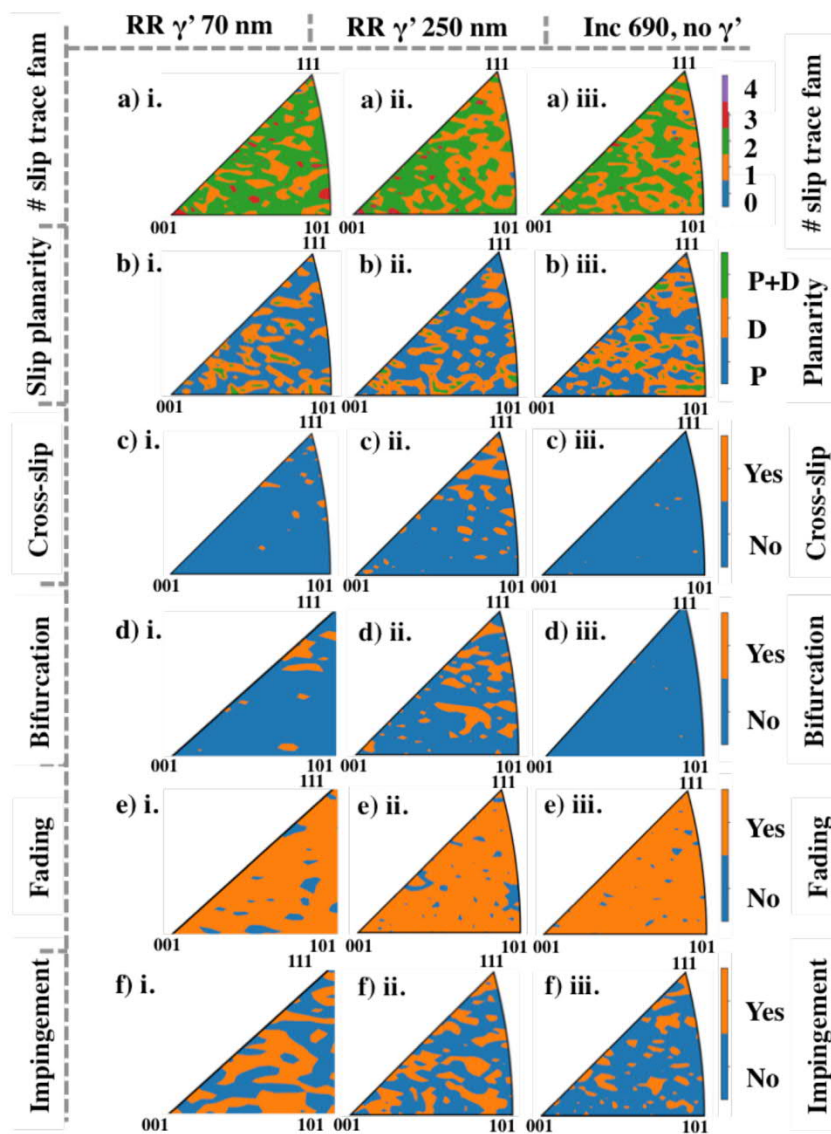
Fig. 13. The slip character distributions in Fig. 12 plotted on IPFs from the loading direction, smoothed. (For interpretation of the references to colour in this figure legend, the reader is referred to the web version of this article.)

it. Conversely, the precipitation-strengthened alloys, the slip plane softening encourages strain localisation that results in slip band widths on the scale of the precipitates and therefore cross-slip on the scale of the precipitates.

3.5. Deformation related defect structures

Fig. 6 shows cECCI analysis of the interaction of dislocations with γ' particles. There is evidence for particle shearing in both the fine- and coarse-γ' alloy variants. However, the coarse-γ' variant shows more dislocation-γ' interaction at the γ/γ' interfaces, pileups at the interface and parallel co-planar slip within a single slip trace. In the fine-γ' variant there is deformation between the slip bands, shown in Fig. 6(c), in the form of coupled dislocations (denoted SC in the figure) and some bowing around γ'. This coupling suggests particle shear and, as the coupling is short in comparison to the size of the γ', the shearing is in the strong coupling regime [1,15].

Fig. 14 shows cECCI analysis of slip band interactions in each of the three alloy variants using the $g = \bar{1}1\bar{1}$ diffracting vector; the related HRDIC ε_{eff} maps are shown additionally. In the fine- and coarse-γ' variants a higher intensity is observed where non co-planar slip bands intersect as indicated by red arrows in Fig. 14(a),

suggesting larger defect density at these intersections. This does not occur in the solution-strengthened alloy. The example in Fig. 14(c) and (d) shows a grain with two slip trace families aligned with the (1 $\bar{1}$1) and the ($\bar{1}$11) slip traces, and no noticeable accumulation of defects at their intersection. In fact, the ($\bar{1}$11) slip bands are barely visible in the cECCI, possibly because those slip bands have a lower strain magnitude and/or the dislocations on those slip bands have been swept away by dislocations gliding in the (1$\bar{1}$1) slip bands. In any case, no significant accumulation of defects at slip band interactions is typical for this alloy, regardless of slip band strength.

Slip band impingement on a grain boundary can induce slip in the neighbouring grain. This can occur by the slip in one grain inducing stress concentrations in the neighbouring grain, which are accommodated by slip in a compatible slip system, effectively transferring slip from one grain to the other. An example of this slip transfer is given in Fig. 15 for the fine-γ' variant. In part d), the bottom grain shows sharp, planar slip along the (11$\bar{1}$) and the ($\bar{1}$11) traces and the neighbouring top grain shows plumes or 'micro-volumes' [54,79] of misorientation ahead of those slip traces. These plumes are roughly orientated along the (010) in the top grain and are therefore not directly propagating into slip bands. However, we do observe {111} slip, which is just visible in the neighbouring top grain along that
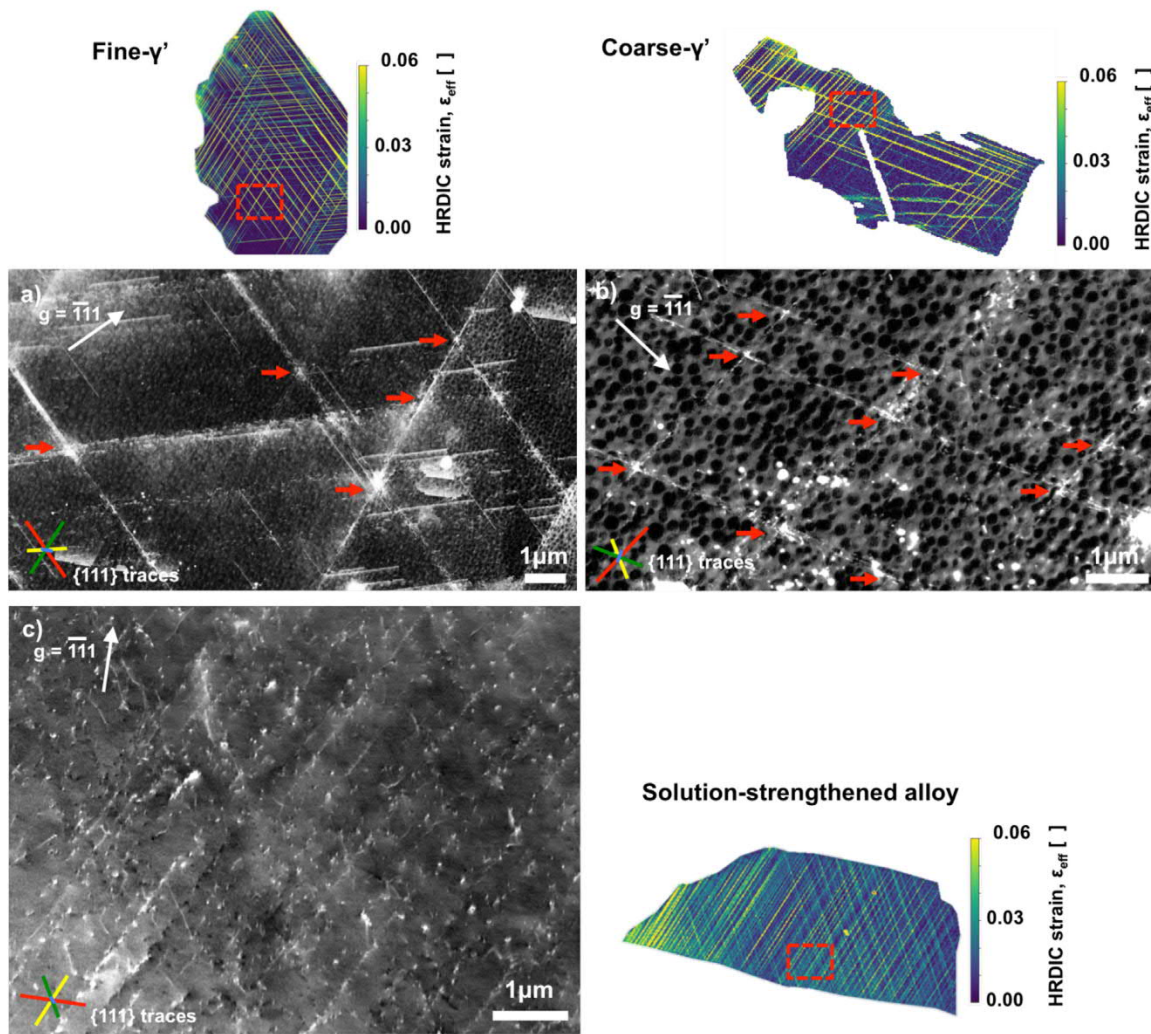
Fig. 14. ECCI analysis of the interactions between non co-planar slip bands in a) the fine-γ' variant, b) the coarse- γ' variant and c—d) the solid solution alloy using the g = 11 1 diffracting vector. Part d) is a higher magnification image of the red dotted region in part c). Red arrows highlight greater defect intensity at the slip band intersections. The {111} slip traces are shown for each image as four coloured lines, the length of the line representing the angular distance between the plane normal and the sample normal. (For interpretation of the references to colour in this figure legend, the reader is referred to the web version of this article.)

grain's blue (111) and green ($\bar{1}$11) slip traces. The (010) plume strains are so well accommodated for that they are not observed in the HRDIC strain data, only in the EBSD misorientation data, and no dislocations are observed at the edges of the plumes. Together, these observations suggest that the (010) plumes are a result of local elastic strain with no evidence of geometrically necessary dislocations to accommodate that strain.

Slip band impingement on a grain boundary can induce misorientations at the boundary in the parent grain and poor slip transfer in the neighbour, as shown in Fig. 16(a) for the coarse-γ' variant. There is significant pileup at the grain boundary in the upper grain and its lower neighbour has an active slip system that is almost perpendicular to the direction of strain. This poor slip transfer results in deformation localisation at both sides of the grain boundary. Conversely, slip band impingement in the solution-strengthened alloy does not have such a severe effect. We show an example of this in Fig. 16(b), where the slip impingement from the upper grain produces no misorientation in the upper grain but its neighbour shows slip band fading and large misorientations even though the slip direction seems well aligned. The comparison between these two examples in Fig. 16 shows how higher dislocation density within fewer slip bands can lead to more severe strain localisation at the grain boundary and that a high misorientation does not necessarily mean high slip activity. Impingement creates grain boundary strain localisation for the grain

Fig. 16 because of poor slip transfer. Conversely, the impingement at the boundary in the grain in Fig. 15 does not show high strain localisation because the slip transfer is efficient. In the fine-γ' variant, the magnitude of the strain in the slip traces is higher than in the other alloys and so the slip band impingement on grain boundaries in this variant creates greater strain localisation at the boundary and stress concentrations in its neighbour.

The main way in which slip bands interact with grain boundaries in all three alloy variants is by fading towards them. In the γ'-strengthened alloys, this mechanism is especially prevalent in grains that contain multiple non co-planar slip systems operating, which suggests that the interaction of non co-planar slip bands may prevent glide from progressing as far as the grain boundary. Slip band fading is closely associated with a local misorientation of nearly 2°, caused by the gradient in plastic strain. This is shown in Fig. 17 for the solution-strengthened alloy. The insets of HRDIC strain and EBSD misorientation in Fig. 17(a) and (b), respectively, show that while the plastic slip fades the lattice distortion is large. That is because the majority of the grain is undergoing plastic rotation in one direction, whilst the bottom part towards the boundary is not, causing a significant misorientation relative to the mean orientation. Interestingly, there are some dislocations observed in this region but these are not spatially distributed in a way that is consistent with the distribution of misorientation. A quarter of all visible dislocations will be invisible
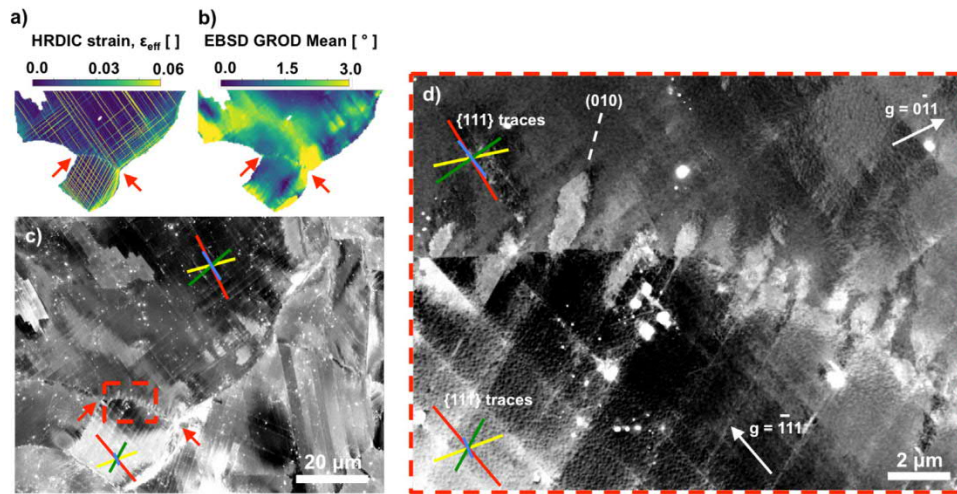
Fig. 15. ECCI analysis of a deformed grain couple in the sample RR1000 with γ' 70 nm. Parts a) and b) show the HRDIC effective strain and EBSD misorientation data, respectively. Red arrows indicate the edges of the grain boundary that separates the grain. Part c) is an ECCI image of the same region in parts a) and b). Part d) is a magnified image from the red dotted region in part c). The {111} slip traces are shown for each grain of interest as four coloured lines, the length of the line representing the angular distance between the plane normal and the sample normal. (For interpretation of the references to colour in this figure legend, the reader is referred to the web version of this article.)

at this imaging orientation, but all belong to the same plane, which is unlikely to allow such a 3D rotation. This lack of observable defects associated with the lattice rotation questions the concept of geometrically necessary dislocations (GNDs) between the slip bands that would account for the smooth gradient in misorientation, which is at odds with EBSD-based measures of plasticity and explanations of misorientation as a homogeneous spatial distribution of GNDs. Instead, the dislocations within slip bands decrease in number and increase in spacing as they approach the boundary. These slip band dislocations act as GND pinning points that are associated with the magnitude of the misorientation, but the more homogeneous gradient in misorientation cannot be attributed to resolvable dislocations. This suggests that either the low spatial and angular resolution of Hough transform indexing EBSD is unable to resolve the fine

structure in these cases, that elastic lattice rotation is not insignificant in these cases or both. Similar observations can be made in the γ'-strengthened alloys, although it is more difficult to observe individual dislocations within slip bands due to their interaction with γ'.

One further point to note in the deformation characteristics of the solution-strengthened alloy is that some of the slip bands have a single pair of dislocations at their tips, closer to one another than the spacing of the other dislocations in that slip band, highlighted by arrows in Fig. 17(d) and included as inserts at the top of the figure. This is reminiscent of dislocation pairs shearing long-range ordered precipitates on the nano-scale < 2 nm [80]. However, as this is only one pair at the very tip of the slip band and not multiple pairs, the ordering here is either due to very small precipitates in low volume fraction or short-range order in solid solution.
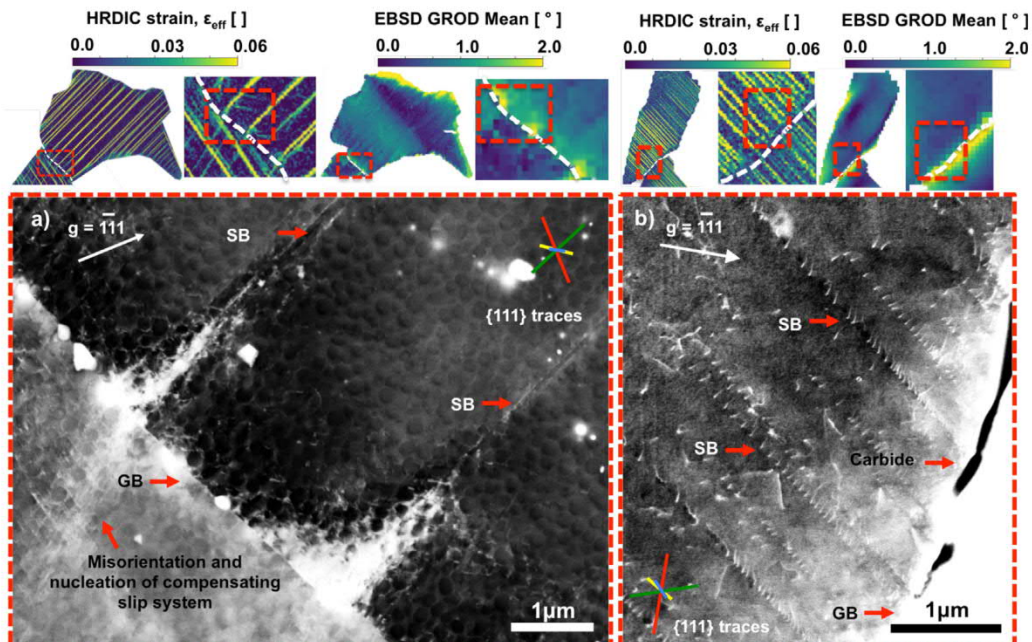

Fig. 16. ECCI analysis of dislocation pile-ups in a) RR1000 coarse-γ' variant and in b) Inconel 690, no γ'. The {111} slip traces are shown for each grain of interest as four coloured lines, the length of the line representing the angular distance between the plane normal and the sample normal. (For interpretation of the references to colour in this figure legend, the reader is referred to the web version of this article.)
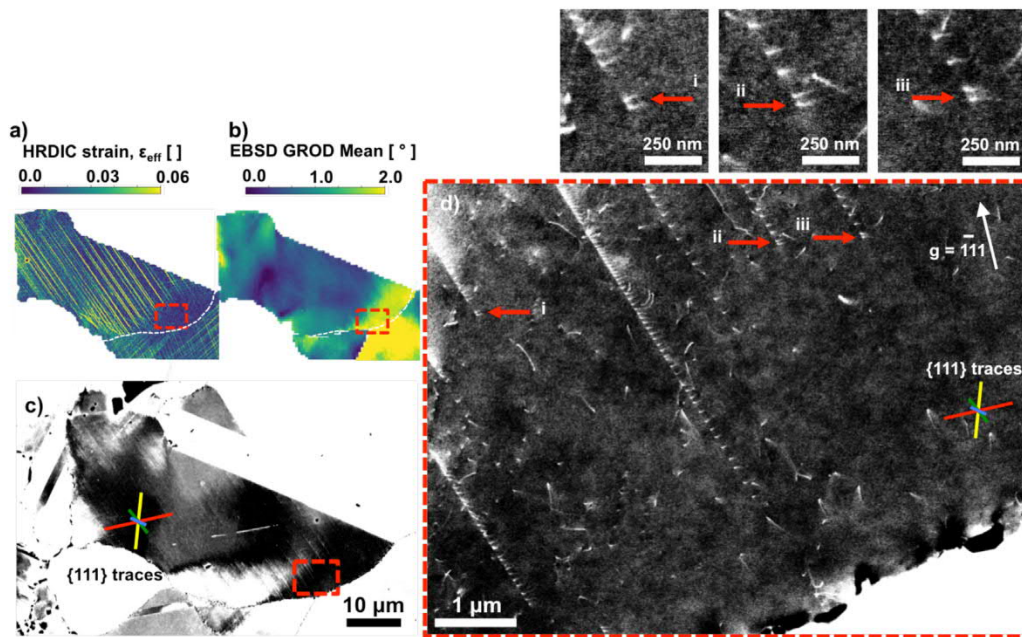
Fig. 17. ECCI analysis of a deformed grain in the sample Inconel 690 with no γ'. Parts a) and b) show the HRDIC effective strain and EBSD misorientation data, respectively. Part c) is an ECCI image of the same region in part a) and b). Part d) is a magnified image from the red dotted region in part c). The {111} slip traces are shown for the grain of interest as four coloured lines, the length of the line representing the angular distance between the plane normal and the sample normal. Short arrows show dislocations in slip bands. Long arrows show dislocation pairs at slip band tips. (For interpretation of the references to colour in this figure legend, the reader is referred to the web version of this article.)

4. Discussion

4.1. Deformation patterning

The presence of γ' drastically changes the alloy yield strength, strain hardening behaviour and ductility. In all the alloys studied here, the planar slip traces are consistent with slip systems that are exclusively $\langle 1\bar{1}0 \rangle \{111\}$ type. Obstacles in the path of dislocation glide increase the stress required for glide [7], which increases the yield strength and promotes elastic dislocation-dislocation interactions that increase strain-hardening. The way in which slip evolves in the presence of obstacles has a marked effect on slip character. The presence of γ' creates more planar, localised deformation on fewer non co-planar slip plane families. Increased slip localisation is related to increased deformation incompatibility between grain neighbours and the emergence of diffuse deformation bands that span many grains. These diffuse strain bands have been known for many decades [81], are not crystallographic [66,67] and have been demonstrated by lower resolution DIC [36,82–84]. However, it is only with the high lateral resolution and wide field of view presented here that we can suggest mechanisms for their formation. We show that the deformation is dominated by planar slip, which impinges on grain boundaries to create rotation at the boundary. This spatial relationship has been shown previously on different length scales: in highly localised shear traces in Mg alloys [85] and ahead of individual slip traces blocked by grain boundaries [41]. As a precursor to cracking, damage accumulation occurs where slip transfer is poor, and so geometric rotations are needed to prevent the nucleation of voids [86]. High angle grain boundaries [87,88] and those that are not of a special coincident site type [89] are known to experience the greatest misorientation due to poor slip transfer. The debate surrounding slip transfer criteria is beyond the scope of the present work [90], but we show that as the grains in the precipitation-strengthened alloys incur more strain their strain distribution becomes more heterogeneous, creating more intense slip bands, more grain boundary impingement and more diffuse hotspots. This is important because the diffuse hotspots are spatially associated with EBSD misorientation hotspots and large lattice rotations are often used to explain local deformation [70–72,91–95],

but we show that the lattice rotations are generally caused by slip band impingement on grain boundaries and are not necessarily spatially coincident with a high strain magnitude. Further, measurable misorientations are not necessarily associated with any slip activity at all or any resolvable GNDs. The misorientation at grain boundaries is more heterogeneous in the precipitation-strengthened alloys, suggesting that more severe lattice rotation is needed to accommodate highly localised slip, in agreement with the lattice rotations associated with greater strain localisation after irradiation in Zr alloys [96]. Conversely, the grains in the solution-strengthened alloy achieve a high mean strain by the quick nucleation of new slip bands, which is more effective in the absence of barriers to glide and when the grain size is small.

More exotic slip characteristics are required to overcome obstacles that induce greater internal stresses, such as cross slip and slip band bifurcation to overcome large precipitates, especially in $\langle 111 \rangle$ grains in which all three active $\langle 110 \rangle$ slip directions can cross slip to three of the four {111} slip planes. Cross-slip has a characteristic activation volume and so it is easier where there is more space between the particles, which is the case for the coarse-γ' variant, leading to wider slip bands and more pile-ups at the γ/γ' interface. The fine-γ' variant has the most heterogeneous strain distribution because these dislocation- interactions are restricted to simple shear.

4.2. Micromechanisms contributing to strength

The dominant contribution to yield strength in the precipitation-strengthened variants is from γ' long-range order (LRO) and it is well established that the strengthening depends on the size and spacing of the particles [97,98]. Slip planarity is achieved in the precipitation-strengthened alloys by the shearing mechanism, which gradually decreases the obstacle size along a given $\langle 1\bar{1}0 \rangle \{111\}$ system by a magnitude equal to $2b$ for each shearing dislocation pair. The shearing process results in a lower stress necessary for glide and therefore glide plane softening, planar slip [99,100] and the greater strain localisation that we observe here.

The strengthening contribution from LRO for the fine-γ' variant is close to the transition between shearing and Orowan looping (see

supplementary material for the calculation) and the greater strength over a solid solution comes from particle shear in the strong coupling regime with some bowing akin to Orowan looping [16]. The cECCI work here supports this calculation as both shearing and looping mechanisms are shown in Fig. 6. Further, similar observations have been made by transmission electron microscopy in Ni-based superalloys of similar size and volume fraction [9,101,102].

For the coarse-γ' variant, the yield stress is lower than that of the fine-γ' variant because there is more space between γ' particles, which results in fewer barriers to slip band formation. However, the γ' themselves are more difficult to shear and so dislocations bypass the particles by the Orowan looping mechanism [16]. The γ' size-dependence of shearing or Orowan mechanisms is well known [3,4]. For large γ' precipitates the partitioning of elastic strain, as measured in neutron diffraction experiments, from the γ phase to the γ' at larger γ' sizes indicates greater plastic deformation in the γ phase and likely Orowan looping [5,11,12,14,15], although looping at much smaller γ' diameters of 39 nm has been observed under certain conditions [6]. For the coarse-γ' variant studied here (see supplementary material for the calculation), strengthening is dominated by LRO shearing in the strong coupling regime (97.5% of a contribution) with a contribution from Orowan looping (2.5% of a contribution). In support of this calculation, both shearing and looping mechanisms have been shown in the cECCI work here in Fig. 6 and in other coarse-γ' microstructures during room temperature deformation [11].

The solution-strengthened alloy contains no LRO but the dislocation pairs that we observe at the head of slip bands constitute evidence for the presence of short-range order (SRO). Dislocation pairing is caused by the creation and then the destruction of the antiphase boundary in secondary phases of LRO as they are sheared by dislocation glide; the number of dislocation pairs, n, gives the obstacle size as $n2b$, where b is the magnitude of the Burgers vector (in the present case $b = 0.248$ nm). While dislocation pairing is generally attributed to LRO, the size of this obstacle in the solution-strengthened alloy is small at ~0.5 nm. This is in the correct range for Ni-Cr couplings in solid solution of MC2-like alloys, constituting SRO microdomains of size 0.5–1 nm [103,104], but approximately twice the size of Ni-Cr and Ni-Co microdomains in heavily alloyed NiCoCr (equal atomic fractions of each constituent) [105]. SRO promotes slip planarity in nickel alloys [106,107] as the leading dislocation(s) remove the local frictional stress due to the SRO, resulting in glide plane softening [99,108]. Traditionally, the low stacking fault energy (SFE) of heavily alloyed Ni is thought to be responsible for slip planarity due to the lack of cross slip available to partial dislocations [73]. However, the fine multi-slip that we define as cross slip, shown in Fig. 9(d), is observed in the solution-strengthened alloy and indeed for all alloys studied here. The oscillatory nature of the SRO results in local variations of the friction stress and therefore hard and soft regions on the order of a few nm. It is in these soft regions that dislocations can nucleate at sources [109]. The slip band then evolves towards the grain boundaries, where dislocation pile-ups cause backstresses that quickly exhaust the dislocation source, instigating the nucleation of new slip bands [80]. Each new slip band experiences the same initial friction stresses due to the SRO, which increases the yield stress relative to a perfectly disordered solid solution and, further, ensures slip planarity and the quick nucleation of many slip bands, resulting in the greater strain homogeneity at the grain scale.

4.3. Micromechanisms contributing to strain-hardening

Slip planarity and greater strain localisation in the precipitation-strengthened alloys increases strain-hardening due to increased local friction stresses because of the elastic interactions between dislocations. These interactions occur at pile-ups at the γ/γ' interface, at grain boundaries, within areas of complex cross-slip, between gliding dislocations and Orowan loops and between dislocations in closely-spaced multiple parallel slip planes within a single slip band. In the coarse-γ' variant these interactions are more common and so the strain-hardening is greater [7,9,110], resulting in higher backstresses on dislocation sources and quicker exhaustion of those sources [111]. Particularly, cross-slip and Orowan looping around large γ' results in greater effective obstacle sizes and higher rates of strain-hardening [7]. In the solution-strengthened alloy the strain-hardening is dominated by long-range elastic stresses, such as the interactions between dislocations in co-planar slip bands and the backstresses arising from pile-ups at boundaries and interfaces [80,112,113], common in FCC systems [80,110,111,114–117]. This mechanism of strain-hardening will also be important in the precipitation-strengthened alloys and especially the fine-γ' variant due to its greater capacity for glide plane softening. Less dislocation-γ' interaction in the fine-γ' accounts for the lower strain-hardening rate in comparison to the coarse-γ' variant. The fine-γ' contains both it's 70 nm intragranular γ' and superfine 10 nm γ'. Although superfine γ' is not thought to contribute to strain-hardening [118], there are chemical differences between the γ' of different sizes [119] and there is much chemical variation at the γ/γ' interface [120], which may affect the interaction of dislocations with γ' and with one another at the interphase boundary. Further, elements common to γ' are segregated to the dislocation line in deformed RR1000 [120] and so chemical variation between different γ' particles may affect the stress field of individual dislocations after they have sheared the particle. These effects are likely more important for the fine-γ' RR1000 variant due to its greater propensity for deformation by particle shear.

The solution-strengthened alloy shows a monotonic decrease in the strain hardening, which is indicative of a single hardening mechanism. The most likely candidate for this mechanism is strain-hardening is through dynamic slip band refinement, i.e. the development of internal stresses that quickly exhaust dislocation sources and necessitates the nucleation of new slip bands [80]. This mechanism occurs due to three main sources of internal local stress: frictional stresses in overcoming short range order, frictional stresses due to the interaction between co-planar slip bands and backstresses at grain boundary pile-ups. As the number of slip bands increases, the elastic interaction between dislocations on different slip bands intensifies and the passing stress increases, increasing the flow stress and maintaining the strain-hardening. However, there must be a competing softening mechanism because the gradient of the flow stress continuously decreases. This second mechanism is likely to involve some slip bands being close enough to one another for mutual annihilation by recombination. In support of this, we demonstrate that slip bands are very closely spaced in this alloy. The significant ductility and strain-hardening capacity of the solution-strengthened alloy is due to the effectiveness of dynamic slip band refinement and the short-range order present in solid solution, which, when coupled with the low stacking fault energy of alloyed Ni, delays the onset of late stage strain-hardening to higher strains.

The precipitation-hardened alloys show a latent peak in the strain-hardening, which has been shown for a similar coarse-γ' variant [15] and in 720Li under tension at room temperature [13]. However, this delayed peak in the strain-hardening rate was not observed previously for a fine-γ' variant [15]. There are two related strain-hardening mechanisms that this could be attributed to. In both the fine- and the coarse-γ' variants substantial backstresses due to grain boundaries give rise to diffuse stain hotspots and mesoscopic deformation bands that span many grains, which may contribute to the latent increase in strain hardening. The second mechanism that will contribute to the latent strain-hardening peak comes from the interaction of non co-planar slip bands. We have shown here that the defect density at slip band intersections is only higher in the precipitation-strengthened alloys. Therefore, the junctions may form due to interactions at the γ/γ' interface. However, junctions have also been shown to affect mechanical behaviour in solid solution, for example,

nano-indentation of Cu single crystals has been used to demonstrate that deformation occurs in bursts via the breakthrough of dislocation pileups at Lomer-Cottrell locks [121]. Such junctions therefore increase strain-hardening, as they are sessile [122] and so they continuously decrease the slip distance as the deformation progresses [123]. While the interaction between non co-planar slip bands does not create locks in the solution-strengthened alloy, such phenomena may occur at higher strains as dislocation density increases, leading to dislocation forest hardening.

An interesting aspect of the strain hardening behaviour in the precipitation-strengthened alloy variants is the precipitous drop in strain-hardening at high strains. As this drop precedes failure, it supports the idea that fracture is of a brittle nature in these special heat-treated conditions. Any discussion on the mechanisms involved based on the work here would be speculative; more deformation mapping in the high strain regime when strain-softening occurs would be useful in this regard.

5. Conclusions

In Nickel-base superalloys, deformation at the microscopic scale is planar and discrete, taking the form of intense slip bands that vary in density and intensity depending on the interactions of dislocations with the microstructure. Impingement of slip bands on grain boundaries creates diffuse regions of strain and associated lattice rotations. At the mesoscopic scale, the diffuse regions form deformation bands that span many neighbouring grains. As these bands are orientated $\sim \pm 53°$ to the load axis they are related to the planarity of the lamella slip but because they span many grains they are non-crystallographic. Site-specific investigations of nanoscale mechanisms are required to confirm suspected local mechanisms of deformation, such as slip trace impingement creating stress concentrations in grain neighbours, and exclude others, such as large misorientations being associated with resolvable GNDs. In comparing the deformation microstructure for the three alloys studied here, we can conclude the following:

The solution-strengthened alloy strain-hardens by a dynamic slip band refinement mechanism due to backstresses that arise from the interaction of slip bands with grain boundaries and other slip bands. At boundaries, the slip bands fade or pile up but the backstresses quickly exhaust the dislocation sources as there is only short-range order in the solid solution that acts as a barrier to new slip band formation. The more gradual build up of backstresses results in more moderate strain-hardening but over a large plasticity range, which results in high ductility.

The γ'-strengthened alloys deform by a glide plane softening mechanism resulting in decreasing resistance to glide through particle shear. These alloys strain-harden more than the solution-strengthened alloy due to higher stresses internal to the grains. These higher stresses arise from dislocation-γ' and dislocation-dislocation interactions at the γ/γ' interface. These interactions necessitate different slip character, such as cross slip and slip band bifurcation, which is especially in grains that are orientated $\langle 111 \rangle$ with respect to the loading direction and particularly in the coarse-γ' variant because of the necessity for cross-slip and Orowan looping to overcome larger γ' obstacles.

The presence of γ' results in more slip band impingement on grain boundaries, creating more diffuse deformation regions and increasing strain hardening further by putting greater backstresses on dislocation sources.

A latent peak in the strain-hardening is observed for the precipitation-strengthened alloys, which must be due to a common mechanism in the fine-γ' and coarse-γ' variants. We suggest this latent peak occurs through two mechanisms: (1.) Higher dislocation densities at the junction between non co-planar slip systems create locks, decreasing the slip distance and increasing backstresses; and (2.)

High slip intensity and more slip band impingement on grain boundaries create a greater density of diffuse strain regions near boundaries, which causes local hardening.

While the work presented here specifically focuses on nickel-base superalloys, it is likely that the findings are more broadly applicable to other highly alloyed precipitation-strengthened materials.

Declaration of Competing Interest

The authors declare that they have no known competing financial interests or personal relationships that could have appeared to influence the work reported in this paper.

Acknowledgements

Supplementary materials

Supplementary material associated with this article can be found in the online version at doi:10.1016/j.actamat.2020.04.004.

References

[1] R.C. Reed, C.M.F. Rae, Physical Metallurgy of the Nickel-Based Superalloys, 5th Ed., Elsevier B.V, 2014, doi: 10.1016/B978-0-444-53770-6.00022-8.

[2] M.C. Hardy, B. Zirbel, G. Shen, R. Shankar, Developing damage tolerance and creep resistance in high strength nickel alloy for disk applications, Superalloys, 2004, pp. 83–90.

[3] B. Reppich, P. Schepp, G. Wehner, Some new aspects concerning particle hardening mechanisms in γ' precipitating nickel base alloys I: theoretical experiments, Acta Metall. 30 (1982) 95–104.

[4] E. Nembach, G. Neite, Precipitation hardening of superalloy by ordered gamma prime particles, Prog. Mater. Sci. 29 (1985) 177–319.

[5] E.M. Francis, B.M.B. Grant, J.Q. Da Fonseca, P.J. Phillips, M.J. Mills, M.R. Daymond, M. Preuss, HT deformation mechanisms in a polycrystalline Ni-base superalloy studied by neutron diffraction and electron microscopy, Acta Mater. 74 (2014) 18–29, doi: 10.1016/j.actamat.2014.04.028.

[6] B.D. Fu, K. Du, G.M. Han, C.Y. Cui, J.X. Zhang, Deformation mechanisms in Co-rich nickel based superalloy with different sizes of gamma prime precipitates, Mater. Lett 152 (2015) 272–275.

[7] W. Mangen, E. Nembach, The effect of grain size on the yield strength of Ni3Al, Acta Metall. 33 (1985) 1587–1591, doi: 10.1016/0001-6160(85)90152-X.

[8] K.K. Sharma, D. Banerjee, S.N. Tewari, Effect of reverse-aging treatment on the microstructure and mechanical properties of Nimonic alloys, Mater. Sci. Eng. 104 (1988) 131–140, doi: 10.1016/0025-5416(88)90414-4.

[9] V. Seetharaman, K.B.S. Rao, D. Sundararaman, P. Rodriguez, Precipitation and tensile deformation behaviour of a nimonic 105 superalloy, Acta Metall 35 (1987) 565–575, doi: 10.1016/0001-6160(87)90180-5.

[10] M.P.P. Jackson, R.C.C. Reed, Heat treatment of UDIMET 720Li: the effect of microstructure on properties, Mater. Sci. Eng., A 259 (1999) 85–97, doi: 10.1016/S0921-5093(98)00867-3.

[11] E.M. Knoche, Influence of the precipitate size on the deformation mechanisms in two nickel-base superalloys, 2001.

[12] M. Preuss, J. Quinta da Fonseca, B. Grant, E. Knoche, R. Moat, M. Daymond, The effect of γ' particle size distribution on the deformation mechanism in an advanced pollycrystalline nickel-base superalloy, Superalloys. TMS (2008) 405–414 (2008).

[13] K. Gopinath, A.K. Gogia, S.V. Kamat, U. Ramamurty, Dynamic strain ageing in Ni-base superalloy 720Li, Acta Mater 57 (2009) 1243–1253, doi: 10.1016/j.actamat.2008.11.005.

[14] B.M.B. Grant, E.M. Francis, J.Q. da Fonseca, M. Preuss, M.R. Daymond, The effect of γ' size and alloy chemistry on dynamic strain ageing in advanced polycrystalline nickel base superalloys, Mater. Sci. Eng. A 573 (2013) 54–61, doi: 10.1016/j.msea.2013.02.027.

[15] B.M.B. Grant, E.M. Francis, J. Quinta Da Fonseca, M.R. Daymond, M. Preuss, Deformation behaviour of an advanced nickel-based superalloy studied by neutron diffraction and electron microscopy, Acta Mater. 60 (2012) 6829–6841, doi: 10.1016/j.actamat.2012.09.005.

[16] D.J. Bacon, U.F. Kocks, R.O. Scattergood, The effect of dislocation self-interaction on the orowan stress, Philos. Mag. 28 (1973) 1241–1263, doi: 10.1080/14786437308227997.

[17] E.I. Galindo-Nava, L.D. Connor, C.M.F. Rae, On the prediction of the yield stress of unimodal and multimodal gamma prime nickel base superalloys, Acta Mater 98 (2015) 377–390.

[18] G. Dieter, Mechanical metallurgy, 1986.

[19] G. Scheunemann-Frerker, H. Gabrisch, M. Feller-Kniepmeier, Dislocation microstructure in a single-crystal nickel-based superalloy after tensile testing at 823 K in the [001]direction, Philos. Mag. A Phys. Condens. Matter, Struct. Defects Mech. Prop 65 (1992) 1353–1368, doi: 10.1080/01418619208205609.

[20] Z.P. Luo, Z.T. Wu, D.J. Miller, The dislocation microstructure of a nickel-base single-crystal superalloy after tensile fracture, Mater. Sci. Eng. A 354 (2003) 358–368, doi: 10.1016/S0921-5093(03)00039-X.

[21] J.X. Zhang, T. Murakumo, H. Harada, Y. Koizumi, T. Kobayashi, Creep deformation mechanisms in some modern single-crystal superalloys, superalloys 2004, Tenth Int. Symp (2004) 189–195, doi: 10.7449/2004/Superalloys_2004_189_195.

[22] C.M.F. Rae, R.C. Reed, Primary creep in single crystal superalloys: origins, mechanisms and effects, Acta Mater 55 (2007) 1067–1081, doi: 10.1016/j.actamat.2006.09.026.

[23] V.A. Vorontsov, L. Kovarik, M.J. Mills, C.M.F. Rae, High-resolution electron microscopy of dislocation ribbons in a CMSX-4 superalloy single crystal, Acta Mater 60 (2012) 4866–4878, doi: 10.1016/j.actamat.2012.05.014.

[24] Z. Shi, X. Wang, S. Liu, J. Li, Low cycle fatigue properties and microstructure evolution at 760 1 C of a single crystal superalloy, Prog. Nat. Sci. Mater. Int 25 (2015) 78–83, doi: 10.1016/j.pnsc.2015.01.009.

[25] X. Wu, P. Wollgramm, C. Somsen, A. Dlouhy, A. Kostka, G. Eggeler, Double minimum creep of single crystal Ni-base superalloys, Acta Mater 112 (2016) 242–260, doi: 10.1016/j.actamat.2016.04.012.

[26] F. Di Gioacchino, J.Q. da Fonseca, An experimental study of the polycrystalline plasticity of austenitic stainless steel, Int. J. Plast 74 (2015) 92–109.

[27] M. Linne, S. Daly, A. Venkataraman, M.D. Sangid, Deformation mechanisms at grain boundaries in polycrystals, 2019. doi:10.11693/hyhz20181000233.

[28] W.Z. Abuzaid, M.D. Sangid, J.D. Carroll, H. Sehitoglu, J. Lambros, Slip transfer and plastic strain accumulation across grain boundaries in Hastelloy X, J. Mech. Phys. Solids. 60 (2012) 1201–1220, doi: 10.1016/j.jmps.2012.02.001.

[29] F. Bourdin, J.C. Stinville, M.P. Echlin, P.G. Callahan, W.C. Lenthe, C.J. Torbet, D. Texier, F. Bridier, J. Cormier, P. Villechaise, T.M. Pollock, V. Valle, Measurements of plastic localization by heaviside-digital image correlation, Acta Mater 157 (2018) 307–325, doi: 10.1016/j.actamat.2018.07.013.

[30] J.C. Stinville, N. Vanderesse, F. Bridier, P. Bocher, T.M. Pollock, High resolution mapping of strain localization near twin boundaries in a nickel-based superalloy, Acta Mater 98 (2015) 29–42.

[31] I. Aubert, N. Saintier, J.M. Olive, F. Plessier, A methodology to obtain data at the slip-band scale from atomic force microscopy observations and crystal plasticity simulations. Application to hydrogen-induced slip localization on AISI 316L stainless steel, Acta Mater 104 (2016) 9–17, doi: 10.1016/j.actamat.2015.11.042.

[32] F.D. León-Cázares, R. Schlütter, T. Jackson, E.I. Galindo-Nava, C.M.F. Rae, A multiscale study on the morphology and evolution of slip bands in a nickel-based superalloy during low cycle fatigue, Acta Mater 182 (2020) 47–59, doi: 10.1016/j.actamat.2019.10.033.

[33] M. Kamaya, J. Quinta da Fonseca, L.M. Li, M. Preuss, Local plastic strain measurement by EBSD, Appl. Mech. Mater 7–8 (2007) 173–179 10.4028/www.scientific.net/AMM.7-8.173.

[34] D. Jorge-Badiola, A. Iza-Mendia, I. Gutiérrez, Evaluation of intragranular misorientation parameters measured by EBSD in a hot worked austenitic stainless steel, J. Microsc 228 (2007) 373–383, doi: 10.1111/j.1365-2818.2007.01850.x.

[35] M. Kamaya, Characterization of microstructural damage due to low-cycle fatigue by EBSD observation, Mater. Charact. 60 (2009) 1454–1462, doi: 10.1016/j.matchar.2009.07.003.

[36] J.L. Walley, R. Wheeler, M.D. Uchic, M.J. Mills, In-situ mechanical testing for characterizing strain localization during deformation at elevated temperatures, Exp. Mech. 52 (2012) 405–416, doi: 10.1007/s11340-011-9499-7.

[37] M.R. Stoudt, L.E. Levine, A. Creuziger, J.B. Hubbard, The fundamental relationships between grain orientation, deformation-induced surface roughness and strain localization in an aluminum alloy, Mater. Sci. Eng. A 530 (2011) 107–116, doi: 10.1016/j.msea.2011.09.050.

[38] Z. Wang, H. Xue, D. Zhao, Microstructure evolution and surface cracking behavior of superheavy forgings during hot forging, Adv. Mater. Sci. Eng (2018) 1–10.

[39] M.F. Ashby, The deformation of plastically non-homogeneous materials, Philos. Mag. 21 (1970) 399–424, doi: 10.1080/14786437008238426.

[40] L.P. Evers, D.M. Parks, W.A.M. Brekelmans, M.G.D. Geers, Crystal plasticity model with enhanced hardening by geometrically necessary dislocation accumulation, J. Mech. Phys. Solids. 50 (2002) 2403–2424, doi: 10.1016/S0022-5096(02)00032-7.

[41] Y. Guo, T.B. Britton, A.J. Wilkinson, Slip band – grain boundary interactions in commercial-purity titanium, Acta Mater 76 (2014) 1–12, doi: 10.1016/j.actamat.2014.05.015.

[42] B. Larrouy, P. Villechaise, J. Cormier, O. Berteaux, Grain boundary – slip bands interactions : impact on the fatigue crack initiation in a polycrystalline forged Ni-based superalloy, Acta Mater. 99 (2015) 325–336, doi: 10.1016/j.actamat.2015.08.009.

[43] J.C. Stinville, W.C. Lenthe, J. Miao, T.M. Pollock, A combined grain scale elastic-plastic criterion for identification of fatigue crack initiation sites in a twin containing polycrystalline nickel-base superalloy, Acta Mater. 103 (2016) 461–473, doi: 10.1016/j.actamat.2015.09.050.

[44] F. Di Gioacchino, J. Quinta da Fonseca, Plastic strain mapping with sub-micron resolution rsing digital image correlation, Exp. Mech. 53 (2013) 743–754, doi: 10.1007/s11340-012-9685-2.

[45] S.I. Wright, M.M. Nowell, D.P. Field, A review of strain analysis using electron backscatter diffraction, Microsc. Microanal. 17 (2011) 316–329.

[46] S. Zaefferer, N. Elhami, Theory and application of electron channeling contrast imaging under controlled diffraction conditions, Acta Mater. 75 (2014) 20–50.

[47] A. Harte, M. Atkinson, M. Preuss, J.Q. da Fonseca, High resolution deformation data from the surface of a Nickel-based superalloy: coarse precipitates, Zenodo (2020) http://doi.org/10.5281/zenodo.3691903 .

[48] A. Harte, M. Atkinson, M. Preuss, J.Q. da Fonseca, High resolution deformation data from the surface of a Nickel-based superalloy: fine precipitates, Zenodo (2020) https://doi.org/10.5281/zenodo.3691931 .

[49] A. Harte, M. Atkinson, M. Preuss, J.Q. da Fonseca, High resolution deformation data from the surface of a Nickel-based alloy: solid solution, Zenodo (2020) https://doi.org/10.5281/zenodo.3691937 .

[50] S. Preibisch, S. Saalfeld, P. Tomancak, Globally optimal stitching of tiled 3D microscopic image acquisitions, Bioinformatics 25 (2009) 1463–1465, doi: 10.1093/bioinformatics/btp184.

[51] LaVision, DaVis, (2018). http://www.lavision.de/en/company.php(accessed October 1, 2018).

[52] D. Lunt, R. Thomas, M. Roy, J. Duff, M. Atkinson, P. Frankel, M. Preuss, J. Quinta da Fonseca, Comparison of sub-grain scale digital image correlation calculated using commercial and open-source software packages, Mater. Charact. 163 (2020) 1–14 110271, doi: 10.1016/j.matchar.2020.110271.

[53] J.C. Stinville, P.G. Callahan, M.A. Charpagne, M.P. Echlin, V. Valle, T.M. Pollock, Direct measurements of slip irreversibility in a nickel-based superalloy using high resolution digital image correlation, Acta Mater. 186 (2020) 172–189, doi: 10.1016/j.actamat.2019.12.009.

[54] J.C. Stinville, M.P. Echlin, D. Texier, F. Bridier, P. Bocher, T.M. Pollock, Sub-grain scale digital image correlation by electron microscopy for polycrystalline materials during elastic and plastic deformation, Exp. Mech (2015), doi: 10.1007/s11340-015-0083-4.

[55] S. van der Walt, S.C. Colbert, G. Varoquax, The NumPy array: a structure for efficient numerical computation, Comput. Sci. Eng. March/Apri (2011) 22–30.

[56] D. Hunter, Matplotlib J., A 2D Graphics Environment, Comput. Sci. Eng. (2007) 90–95 May/June .

[57] M. Atkinson, R. Thomas, A. Harte, P. Crowther, J.Q. da Fonseca, DefDAP, Deformation data analysis in Python, Zenodo (2020) https://doi.org/10.5281/zenodo.3688097 .

[58] J.H. Cho, A.D. Rollett, K.H. Oh, Determination of a mean orientation in electron backscatter diffraction measurements, Metall. Mater. Trans. A Phys. Metall. Mater. Sci. 36 (2005) 3427–3438, doi: 10.1007/s11661-005-0016-4.

[59] A. Melcher, A. Unser, M. Reichhardt, B. Nestler, Conversion of EBSD data by a quaternion based algorithm to be used for grain structure simulations, Tech. Mech. 30 (2009) 401–413.

[60] D. Rowenhorst, A.D. Rollett, G.S. Rohrer, M. Groeber, M. Jackson, P.J. Konijnenberg, M. De Graef, Consistent representations of and conversions between 3D rotations, Model. Simul. Mater. Sci. Eng. (2015) 23, doi: 10.1088/0965-0393/23/8/083501.

[61] S.I. Wright, S. Suzuki, M.M. Nowell, In situ EBSD observations of the evolution in crystallographic orientation with deformation, JOM 68 (2016) 2730–2736, doi: 10.1007/s11837-016-2084-x.

[62] G. Nolze, Image distortions in SEM and their influences on EBSD measurements, Ultramicroscopy 107 (2007) 172–183, doi: 10.1016/j.ultramic.2006.07.003.

[63] F. Strub, M.-A. Charpagne, T.M. Pollock, Correction of electron back-scattered diffraction datasets using an evolutionary algorithm, Pre-Print (2019) http://arxiv.org/abs/1903.02982 .

[64] M.A. Linne, S. Daly, Data clustering for the high-resolution alignment of microstructure and strain fields, Mater. Charact. 158 (2019) 109984, doi: 10.1016/j.matchar.2019.109984.

[65] R. Jiang, D.J. Bull, A. Evangelo, A. Harte, F. Pierron, I. Sinclair, G. McColvin, M. Preuss, X.T. Hu, Y.D. Song, P.A.S. Reed, Strain accumulation and fatigue crack initiation at pores and carbides in a SX superalloy at room temperature, submitted. (2018).

[66] N. Jia, P. Eisenlohr, F. Roters, D. Raabe, X. Zhao, Orientation dependence of shear banding in fcc single crystals, Acta Mater. 60 (2012) 3415–3434.

[67] N. Jia, F. Roters, P. Eisenlohr, C. Kords, D. Raabe, Non-crystallographic shear banding in crystal plasticity FEM simulations: example of texture evolution in α-brass, Acta Mater. 60 (2012) 1099–1115, doi: 10.1016/j.actamat.2011.10.047.

[68] A. Harte, M. Atkinson, M. Preuss, J. Quinta da Fonseca, A statistical study of the relationship between plastic strain and lattice misorientation on the surface of a deformed Ni-base superalloy, Zenodo (2020), doi: 10.5281/zenodo.3701816.

[69] N.P. Gurao, S. Suwas, Generalized scaling of misorientation angle distributions at meso-scale in deformed materials, Sci. Rep. 4 (2014) 1–6, doi: 10.1038/srep05641.

[70] C. Schayes, J. Bouquerel, J.B. Vogt, F. Palleschi, S. Zaefferer, A comparison of EBSD based strain indicators for the study of Fe-3Si steel subjected to cyclic loading, Mater. Charact. 115 (2016) 61–70, doi: 10.1016/j.matchar.2016.03.020.

[71] S. Rui, Y. Shang, W. Qiu, L. Niu, H. Shi, Fracture mode identification of low alloy steels and cast irons by electron back-scattered diffraction misorientation analysis, J. Mater. Sci. Technol. 33 (2017) 1582–1595.

[72] J. Bai, S. Ritter, H.-P. Seifert, S. Virtanen, Stress corrosion cracking initiation and short crack growth behavior in Alloy 182 weld metal under simulated BWR/HWC conditions, Corros. Sci. 131 (2018) 208–222.

[73] D. Hull, D.J. Bacon, Intorduction to Dislocations, 4th ed., 2001.

[74] S.I. Wright, D.P. Field, Recent studies of local texture and its influence on failure, Mater. Sci. Eng. A 257 (1998) 165–170, doi: 10.1016/S0921-5093(98)00835-1.

[75] A. Telang, A.S. Gill, M. Kumar, S. Teysseyre, D. Qian, S.R. Mannava, V.K. Vasudevan, Iterative thermomechanical processing of alloy 600 for improved resistance to corrosion and stress corrosion cracking, Acta Mater. 113 (2016) 180–193, doi: 10.1016/j.actamat.2016.05.009.

[76] A. King, W. Ludwig, M. Herbig, J.Y. Buffire, A.A. Khan, N. Stevens, T.J. Marrow, Three-dimensional in situ observations of short fatigue crack growth in magnesium, Acta Mater. 59 (2011) 6761–6771, doi: 10.1016/j.actamat.2011.07.034.

[77] Z. Xu, M. Liu, Z. Jia, H.J. Roven, Effect of cryorolling on microstructure and mechanical properties of a peak-aged AA6082 extrusion, J. Alloys Compd 695 (2017) 827–840, doi: 10.1016/j.jallcom.2016.10.135.

[78] A.D. Kammers, S. Daly, Digital image correlation under scanning electron microscopy: methodology and validation, Exp. Mech. 53 (2013) 1743–1761, doi: 10.1007/s11340-013-9782-x.

[79] P. Villechaise, J. Cormier, T. Billot, J. Mendez, Mechanical behaviour and damage processes of Udimet 20Li: influence of localized plasticity at grain boundaries, Superalloys 2012 12th Int. Symp. Superalloys, 2012, pp. 15–24.

[80] E. Welsch, D. Ponge, S.M. Hafez Haghighat, S. Sandlöbes, P. Choi, M. Herbig, S. Zaefferer, D. Raabe, Strain hardening by dynamic slip band refinement in a high-Mn lightweight steel, Acta Mater. 116 (2016) 188–199, doi: 10.1016/j.actamat.2016.06.037.

[81] K.G. Davis, E. Teghtsoonian, A. Lu, Slip band continuity across grain boundaries i aluminium, Acta Metall. 14 (1966) 1677.

[82] M.A. Tschopp, B.B. Bartha, W.J. Porter, P.T. Murray, S.B. Fairchild, Microstructure-Dependent local strain behavior in polycrystals through In-Situ scanning electron microscope tensile experiments, Metall. Mater. Trans. A Phys. Metall. Mater. Sci. 40 (2009) 2363–2368, doi: 10.1007/s11661-009-9938-6.

[83] J. Jiang, J. Yang, T. Zhang, J. Zou, Y. Wang, F.P.E. Dunne, T.B. Britton, Microstructurally sensitive crack nucleation around inclusions in powder metallurgy nickel-based superalloys, Acta Mater. 117 (2016) 333–344, doi: 10.1016/j.actamat.2016.07.023.

[84] C.C. Tasan, J.P.M. Hoefnagels, M. Diehl, D. Yan, F. Roters, D. Raabe, Strain localization and damage in dual phase steels investigated by coupled in-situ deformation experiments and crystal plasticity simulations, Int. J. Plast. 63 (2014) 198–210, doi: 10.1016/j.ijplas.2014.06.004.

[85] F. Wang, S. Sandlöbes, M. Diehl, L. Sharma, F. Roters, D. Raabe, In situ observation of collective grain-scale mechanics in Mg and Mg-rare earth alloys, Acta Mater. 80 (2014) 77–93, doi: 10.1016/j.actamat.2014.07.048.

[86] T.R. Bieler, P. Eisenlohr, F. Roters, D. Kumar, D.E. Mason, M.A. Crimp, D. Raabe, The role of heterogeneous deformation on damage nucleation at grain boundaries in single phase metals, Int. J. Plast. 25 (2009) 1655–1683, doi: 10.1016/j.ijplas.2008.09.002.

[87] K.T. Aust, N.K. Chen, Effect of orientation on the plastic deformation of aluminum single crystals and bicrystals, Acta Metall. 2 (1954) 632, doi: 10.1007/BF03398471.

[88] S. Zaefferer, J.C. Kuo, Z. Zhao, M. Winning, D. Raabe, On the influence of the grain boundary misorientation on the plastic deformation of aluminum bicrystals, Acta Mater. 51 (2003) 4719–4735, doi: 10.1016/S1359-6454(03)00259-3.

[89] K. Hirayama, K. Nagai, H. Fujiwara, H. Miyamoto, Effect of grain boundary structure on misorientation change of pure copper bicrystals pressed by one-pass equal-channel angular pressing, Mater. Trans. 54 (2013) 1077–1082, doi: 10.2320/jinstmet.JA201202.

[90] E. Bayerschen, A.T. McBride, B.D. Reddy, T. Böhlke, Review on slip transmission criteria in experiments and crystal plasticity models, J. Mater. Sci. 51 (2016) 2243–2258, doi: 10.1007/s10853-015-9553-4.

[91] K. Yvell, T.M. Grehk, P. Hedström, A. Borgenstam, G. Engberg, Microstructure development in a high-nickel austenitic stainless steel using EBSD during in situ tensile deformation, Mater. Charact. 135 (2018) 228–237, doi: 10.1016/j.matchar.2017.11.046.

[92] J.P. Escobedo, D. Dennis-Koller, E.K. Cerreta, B.M. Patterson, C.A. Bronkhorst, B.L. Hansen, D. Tonks, R.A. Lebensohn, Effects of grain size and boundary structure on the dynamic tensile response of copper, J. Appl. Phys. (2011) 110, doi: 10.1063/1.3607294.

[93] S. Birosca, The deformation behaviour of hard and soft grains in RR1000 nickel-based superalloy, IOP Conf. Ser. Mater. Sci. Eng 82 (2015) 012033, doi: 10.1088/1757-899X/82/1/012033.

[94] K. Mukahiwa, F. Scenini, M.G. Burke, N. Platts, D.R. Tice, J.W. Stairmand, Corrosion fatigue and microstructural characterisation of Type 316 austenitic stainless steels tested in PWR primary water, Corros. Sci. 131 (2018) 57–70, doi: 10.1016/j.corsci.2017.10.022.

[95] S. Tachibana, Y. Kuronuma, T. Yokota, K. Yamada, Y. Moriya, C. Kami, Effect of hot rolling and cooling conditions on intergranular corrosion behavior in Alloy625 clad steel, Corros. Sci. 99 (2015) 125–133, doi: 10.1016/j.corsci.2015.06.028.

[96] R. Thomas, D. Lunt, M.D. Atkinson, J. Quinta da Fonseca, M. Preuss, F. Barton, J. O'Hanlon, P. Frankel, Characterisation of irradiation enhanced strain localisation in a zirconium alloy, Materialia 5 (2019) 100248, doi: 10.1016/j.mtla.2019.100248.

[97] R.C. Reed, The superalloys: fundamentals and applications, Cambridge University Press, New York, 2006.

[98] T. Gladman, Precipitation hardening in metals, Mater. Sci. Technol. 15 (1999) 30–36, doi: 10.1179/026708399773002782.

[99] V. Gerold, H.P. Karnthaler, On the origin of planar slip in F.C.C. alloys, Acta Metall. 37 (1989) 2177–2183.

[100] P.M. Hazzledine, The mobility of dislocation groups, Philos. Mag. 18 (1968) 1033–1039, doi: 10.1080/14786436808227523.

[101] X. Lv, F. Sun, J. Tong, S. Zhang, Q. Feng, J. Zhang, Dislocation configurations and stress distribution along the transverse axis of turbine blade body, J. Mater. Eng. Perform. 24 (2015) 4620–4625, doi: 10.1007/s11665-015-1774-9.

[102] X. Lv, F. Sun, J. Tong, Q. Feng, J. Zhang, Paired dislocations and their interactions with γ′ particles in polycrystalline superalloy GH4037, J. Mater. Eng. Perform. 24 (2015) 143–148, doi: 10.1007/s11665-014-1307-y.

[103] F. Pettinari, M. Prem, G. Krexner, P. Caron, A. Coujou, H.O.K. Kirchner, N. Clemént, Local order in industrial and model γ phases of superalloys, Acta Mater 49 (2001) 2549–2556, doi: 10.1016/S1359-6454(01)00103-3.

[104] F. Pettinari-Sturmel, A. Coujou, N. Clemént, The fluctuation of short-range order evidenced by mobile dislocations in the γ-phase of a nickel-based superalloy, Mater. Sci. Eng. A 400–401 (2005) 114–117, doi: 10.1016/j.msea.2005.02.072.

[105] F.X. Zhang, S. Zhao, K. Jin, H. Xue, G. Velisa, H. Bei, R. Huang, J.Y.P. Ko, D.C. Pagan, J.C. Neuefeind, W.J. Weber, Y. Zhang, Local structure and short-range order in a NiCoCr solid solution alloy, Phys. Rev. Lett 118 (2017) 1–6, doi: 10.1103/PhysRevLett.118.205501.

[106] K. Wolf, H.-J. Gudladt, H.A. Calderon, G. Kostorz, Transition between planar and wavy slip in cyclically deformed short-range ordered alloys, Acta Metall. Mater 42 (1994) 3759–3765.

[107] N.R. Dudova, R.O. Kaibyshev, Short-range ordering and mechanical properties of a Ni-20%Cr alloy, J, Phys. Conf. Ser. 240 (2010) 3–7, doi: 10.1088/1742-6596/240/1/012081.

[108] M. Jouiad, F. Pettinari, N. Clément, A. Coujou, Dynamic friction stresses in the γ phase of a nickel-based superalloy, Philos. Mag. A Phys. Condens. Matter, Struct. Defects Mech. Prop. 79 (1999) 2591–2602, doi: 10.1080/01418619908212011.

[109] F. Pettinari-Sturmel, C. Coupeau, N. Clément, A. Coujou, Activation of dislocation sources in γ-phases of nickel-base superalloys studied by use of atomic-force microscopy and transmission electron microscopy, Mater. Sci. Eng. A 387–389 (2004) 103–108, doi: 10.1016/j.msea.2004.02.084.

[110] B.Y. Welham, H. Coi, Effect of aging treatment and tensile properties of Udimet 520 and Ni- 6.38% Al alloy, Trans. JIM 15 (1974) 24–31.

[111] M.J. Yao, E. Welsch, D. Ponge, S.M.H. Haghighat, S. Sandlobes, P. Choi, M. Herbig, I. Bleskov, T. Hickel, M. Lipinska-Chwalek, P. Shanthraj, C. Scheu, S. Zaefferer, B. Gault, D. Raabe, Strengthening and strain hardening mechanisms in a precipitation- hardened high-Mn lightweight steel, Acta Mater 140 (2017) 258–273, doi: 10.1016/j.actamat.2017.08.049.

[112] E. Smith, The by-passing of an obstacle by a group of coplanar dislocations, Philos. Mag 22 (1970) 1161–1173, doi: 10.1080/14786437008226924.

[113] R. Smallman, A.H.W. Ngan, Modern physical metallurgy, Elsevier Ltd. (2014), doi: 10.1016/C2011-0-05565-5.

[114] L.R. Cornwell, J.D. Embury, G.R. Purdy, The deformation of single crystals of the Ni-Ni3Al system, Acta Metall. 18 (1970) 1217–1223.

[115] A. Soussan, S. Degallaix, T. Magnin, Work-hardening behaviour of nitrogen-alloyed austenitic stainless steels, Mater. Sci. Eng. A 142 (1991) 169–176, doi: 10.1016/0921-5093(91)90655-7.

[116] J.D. Yoo, S.W. Hwang, K.T. Park, Factors influencing the tensile behavior of a Fe-28Mn-9Al-0.8C steel, Mater, Sci. Eng. A. 508 (2009) 234–240, doi: 10.1016/j.msea.2008.12.055.

[117] G. Sun, Y. Zhang, S. Sun, J. Hu, Z. Jiang, C. Ji, Materials science & engineering a plastic flow behavior and its relationship to tensile mechanical properties of high nitrogen nickel-free austenitic stainless steel, Mater. Sci. Eng. A 662 (2016) 432–442, doi: 10.1016/j.msea.2016.03.057.

[118] R.R. Jensen, J.K. Tien, Temperature and strain rate dependence of stress-strain behavior in a nickel-base superalloy, Met. Trans. A 16 (1985) 1049–1068.

[119] Y.Q. Chen, T.J.a Slater, E.a Lewis, E.M. Francis, M.G. Burke, M. Preuss, S.J. Haigh, Measurement of size-dependent composition variations for gamma prime (γ′) precipitates in an advanced nickel-based superalloy, Ultramicroscopy 144C (2014) 1–8, doi: 10.1016/j.ultramic.2014.04.001.

[120] P.A.J. Bagot, O.B.W. Silk, J.O. Douglas, S. Pedrazzini, D.J. Crudden, T.L. Martin, M.C. Hardy, M.P. Moody, R.C. Reed, An atom probe tomography study of site preference and partitioning in a nickel-based superalloy, Acta Mater. 125 (2017) 156–165, doi: 10.1016/j.actamat.2016.11.053.

[121] N. Wieczorek, G. Laplanche, J.K. Heyer, A.B. Parsa, J. Pfetzing-Micklich, G. Eggeler, Assessment of strain hardening in copper single crystals using in situ SEM microshear experiments, Acta Mater. 113 (2016) 320–334, doi: 10.1016/j.actamat.2016.04.055.

[122] C. Monier, C. Bertrand, J.-P. Dallas, M.-F. Trichet, M. Cornet, P. Veyssière, Transmission electron microscopy analysis of the early stages of damage in a γ/γ′ nickel-based alloy under low cycle fatigue, Mater. Sci. Eng. A 188 (1994) 133–139, doi: 10.1016/0921-5093(94)90364-6.

[123] A. Seeger, J. Diehl, S. Mader, H. Rebstock, Work-hardening and work-softening of face-centred cubic metal crystals, Philos. Mag. 2 (1957) 323–350, doi: 10.1080/14786435708243823.